

# **Phase Evolution in Methylammonium Tin Halide Perovskites with Variable Temperature Solid-State $^{119}\text{Sn}$ NMR Spectroscopy**

Michelle Ha<sup>1</sup>, Abhoy Karmakar<sup>1</sup>, Guy M. Bernard<sup>1</sup>, Enoc Basilio<sup>1</sup>, Arun Krishnamurthy<sup>2</sup>, Abdelrahman M. Askar<sup>3</sup>, Karthik Shankar<sup>3</sup>, Scott Kroecker<sup>2</sup> and Vladimir K. Michaelis<sup>1\*</sup>

1. Department of Chemistry, University of Alberta, Edmonton, Alberta, T6G 2G2, Canada
2. Department of Chemistry, University of Manitoba, Winnipeg, Manitoba, R3T 2N2 Canada
3. Department of Electrical and Computer Engineering, University of Alberta, Edmonton, Alberta, T6G 1H9, Canada

## ABSTRACT

Hybrid organic-inorganic metal halide perovskite materials are an emerging class of materials that could profoundly change the optoelectronic and solar absorber research fields and have far-reaching applications. Unfortunately, the leading solar absorbing candidates are lead-containing materials and suffer from chemical instability, eventually decomposing, resulting in detrimental long-term environmental concerns. A series of non-toxic group 14 Sn(II)-based hybrid organic-inorganic metal halide perovskites is investigated using variable-temperature solid-state nuclear magnetic resonance (NMR) spectroscopy to examine their unique phases that appear between 150 and 540 K. Each phase of the  $\text{MASnX}_3$  ( $\text{MA}^+ = \text{CH}_3\text{NH}_3^+$  and  $\text{X}^- = \text{Cl}^-, \text{Br}^-$  or  $\text{I}^-$ ) series is identified and compared to results from quantum chemical calculations of anionic polyhedron clusters. The analysis of the polyhedra about the Sn center is further related to the measured chemical shift anisotropy present when Sn deviates from octahedral symmetry. We also discuss the rapid degradation of pristine  $\text{MASnI}_3$  over two days using *in situ*  $^{119}\text{Sn}$  NMR. Finally, we report on the  $^1\text{H}$ ,  $^{13}\text{C}$ ,  $^{119}\text{Sn}$  and  $^{207}\text{Pb}$  NMR structural properties of a Sn/Pb mixed B-site ( $\text{MASn}_{0.5}\text{Pb}_{0.5}\text{I}_3$ ) perovskite, demonstrating the sensitivity of the chemical shift to B-site substitution.

## INTRODUCTION

Over the last decade the archetypal hybrid methylammonium lead iodide-based (and related modifications) perovskite has been a disruptive technology as a potentially new solar absorbing material with the photoconversion efficiency increasing from 4 % in 2009 to >25 % in 2019.<sup>1</sup> Extending beyond photovoltaic applications, these materials have exhibited exquisitely tailorable bandgaps, often spanning 2 to 3 eV, by adjusting the cation and/or halide compositions. These favorable optical and electronic properties have attracted their development in various applications such as light emitting diodes (LEDs), lasers, X-ray and  $\gamma$ -ray detectors, photocatalysis, etc.<sup>2-6</sup> Perovskites, with a generic formula of  $ABX_3$ , demonstrate excellent material tunability due to their high degree of elemental substitution in the cation (A and B) and anion (X) positions throughout their three-dimensional crystalline lattice. For example, the A site often incorporates a large inorganic (e.g.,  $Cs^+$ ) or small organic cation (e.g., methylammonium,  $CH_3NH_3^+$ , or formamidinium,  $NH_2CH=NH_2^+$ ); the B site can accommodate  $Pb^{2+}$ ,  $Sn^{2+}$  or  $Ge^{2+}$ ; while the X site can be Cl<sup>-</sup>, Br<sup>-</sup>, I<sup>-</sup> or a mixture of these halides.<sup>7-10</sup> Generally, a material must satisfy a few constraints to be called a perovskite; this includes having a general formula,  $ABX_3$ , the B-site cation being in an octahedral-like coordination environment, and the 3D network being interconnected through corner sharing  $[BX_6]$  octahedra and appropriate tolerance factors.<sup>11</sup>

Although the photoconversion efficiency of  $APbX_3$ -based materials have surpassed other remarkable photovoltaic materials, such as CdTe, CIGS and amorphous Si, certain environmental and stability concerns exist as these materials contain Pb and have been shown to be sensitive to temperature and water, ultimately leading to decomposition into  $PbX_2$ .<sup>12-14</sup> Recently, the environmental impact of lead halide perovskites was demonstrated by measuring the bioavailability of plants in perovskite-contaminated soil.<sup>15</sup> The authors found that the lead contamination due to halide perovskites is ten times more bioavailable compared to other lead contaminants found in soil. Also, when exposing plants to the maximum safety level of perovskites in soil, most of them revealed signs of lead toxicity and plant death, suggesting that the safety level for lead needs to be lowered. To circumvent these degradation and environmental concerns, some researchers have shifted their focus to lead-free Sn-variants as new solar absorbing materials.<sup>16-18</sup> To date these materials have received far less attention primarily due to their initial weaker photoconversion efficiencies and the tendency of  $Sn^{2+}$  to readily oxidize to  $Sn^{4+}$ , ultimately impacting the perovskite structure and optical properties.<sup>19-22</sup> However, studies have shown that tin halide perovskites with a cesium cation produce tunable photoluminescence via halide exchange, as well as photocurrents exceeding 22 mA/cm<sup>2</sup> when  $CsSnI_3$  is used as the absorber in perovskite solar cells.<sup>23,24</sup> Using a mixed Sn-Pb B-site, a research team reported a hybrid perovskite solar cell with a 50:50 ratio of

Sn:Pb ( $\text{CH}_3\text{NH}_3\text{Sn}_{0.5}\text{Pb}_{0.5}\text{I}_3$ ) with a tailorable bandgap and a 4.18 % photoconversion efficiency.<sup>25</sup> Despite the challenges faced with tin-based perovskites, in 2014  $\text{CH}_3\text{NH}_3\text{SnI}_{3-x}\text{Br}_x$  and  $\text{CH}_3\text{NH}_3\text{SnI}_3$  were successfully used as light harvesters; demonstrating the vast potential of tin-based perovskites as potential next-generation, environmentally-friendly solar cell materials.<sup>26,27</sup>

Understanding the underlying physical properties of Sn-based perovskites is vital if one is to obtain the optimum photoconversion properties for these materials. Recently, NMR spectroscopy has been shown to be an impressive analytical method in assessing cation and anion structural and dynamic aspects in relation to hybrid and non-hybrid lead halide perovskites<sup>28-35</sup> that is non-destructive, qualitative and quantitative. Solid-state  $^{119}\text{Sn}$  nuclear magnetic resonance (NMR) spectroscopy can be utilized to assess phase changes and the impact of ion substitution on these Sn-based perovskites. Although many researchers use powder X-ray diffraction (XRD) as their structural analysis method, NMR spectroscopy provides complementary insight into sub-nanometer (local and medium-range) structure, as well as on dynamics, further expanding our understanding of the material's structure-property relationships.

Here we extend this method to hybrid tin-containing halide perovskites as  $^{119}\text{Sn}$  (nuclear spin,  $I = 1/2$ ) has a modest natural abundance of 8.58% and a relatively high magnetogyric ratio of  $-10.0318 \cdot 10^{-7} \text{ rad T}^{-1} \text{ s}^{-1}$ , nearly 1/3 that of  $^1\text{H}$ , making it a sensitive NMR probe nucleus for many materials.<sup>36-42</sup> Using *in situ* variable-temperature  $^{119}\text{Sn}$  NMR spectroscopy ranging from 190 to 540 K, the apparent phase transitions of  $\text{MASnX}_3$ , where  $X = \text{Cl, Br or I}$ , are investigated. Degradation of  $\text{MASnI}_3$  is further examined by the impact on the spectral lineshape of the Sn environment. Furthermore, we compare  $^{119}\text{Sn}$  and  $^{207}\text{Pb}$  NMR characteristics of a mixed B-site  $\text{MA}(\text{Sn}/\text{Pb})\text{I}_3$  candidate with respect to the respective parent phases. Finally, we examine how the chemical shift and anisotropy are impacted by the halide composition and the extended Sn-X polyhedra using anionic cluster quantum chemical calculations.

## EXPERIMENTAL

*Materials and methods:* Tin halide salts,  $\text{SnX}_2$  ( $X = \text{Cl}, \text{Br}$  or  $\text{I}$ ) as well as distilled HI (57%) and  $\text{H}_3\text{PO}_2$  (50%) were purchased from MilliporeSigma. Methylammonium halides (MAX, where  $X = \text{Cl}, \text{Br}$  or  $\text{I}$ ) were sourced from GreatCell Solar (formerly DyeSol). During the course of this research we noticed that different sources (Alfa Aesar vs. Sigma Aldrich) of  $\text{SnI}_2$  might contain approximately 50:50 mixtures of  $\text{SnI}_2$  and  $\text{SnI}_4$  (Figure S1); it is advisable that the starting material be screened using NMR and XRD prior to synthesis as mixtures may result in multiple phases of different methylammonium tin halide and tin halide species.

*Synthesis of the parent phases:*  $\text{MASnX}_3$  parent phases were prepared using either solvent synthesis or solid-state reaction methods, or both, following previous published procedures for  $\text{MASnCl}_3$ ,<sup>43</sup>  $\text{MASnBr}_3$ <sup>44</sup> and  $\text{MASnI}_3$ .<sup>10</sup>

*Synthesis of the mixed B-site phase:* A 100 ml three-necked round bottom flask was charged with a mixture of aqueous HI (6.8 ml, 7.58 M) and aqueous  $\text{H}_3\text{PO}_2$  (1.7 ml, 9.14 M) under an inert atmosphere ( $\text{N}_2$  gas). Prior to the addition of tin and lead iodide the flask was purged for two minutes with  $\text{N}_2$  gas.  $\text{SnI}_2$  (186 mg; 0.5 mmol) and  $\text{PbI}_2$  (231 mg; 0.5 mmol) were added to the solution with a stir bar set to 250 RPM. The temperature of the bright yellow solution was maintained between 80 and 90 °C using a mineral oil heating bath. Solid  $\text{CH}_3\text{NH}_3\text{I}$  (159 mg, 1 mmol) was added to the solution and dissolved immediately. The mixture was heated to 120 °C until the solution was reduced by approximately half its volume and went from yellow to black (approximately 1 h). The stirring and heating sources were removed to allow the black solution to cool to ambient temperature and allowed to sit for 24 h under a nitrogen atmosphere to initiate crystallization from the mother liquor. The product was filtered and washed with degassed ethanol and stored under  $\text{N}_2$ .

*Powder X-ray diffraction (PXRD):* Samples were ground to a powder using an agate mortar and pestle and placed on either plastic sample holders or packed into capillary tubes and sealed ( $\text{MASnI}_3$  and  $\text{MASn}_{0.5}\text{Pb}_{0.5}\text{I}_3$ ). PXRD patterns were collected on an Inel powder diffractometer equipped with a curved position-sensitive detector (CPS 120) and a  $\text{Cu } K_{\alpha 1}$  radiation source. PXRD data were acquired using a Bruker D8 Advance Diffractometer equipped with a  $\text{Cu } K_{\alpha}$  source and Vantec-500 2D detector for  $\text{MASnI}_3$  and  $\text{MASn}_{0.5}\text{Pb}_{0.5}\text{I}_3$ .

*Solid-state nuclear magnetic resonance spectroscopy:* Tin-119 NMR spectra were acquired at a magnetic field strength of 7.05 T (300 MHz  $^1\text{H}$ ) with a Bruker AVANCE 300 spectrometer. Non-spinning and magic-angle spinning (MAS)  $^{119}\text{Sn}$  NMR experiments were undertaken using a 4.0 mm double resonance ( $^1\text{H}/\text{X}$ ) NMR probe, where X was tuned to  $^{119}\text{Sn}$  ( $\omega_0/2\pi = 111.9$  MHz). Spectra were acquired using a Hahn-echo pulse sequence with recycle delays set between 0.5 to 200 s, a  $\gamma\text{B}_1/2\pi$  of 62.5 kHz ( $4.0 \mu\text{s} \pi/2$  pulses) and 264 to 16,384 co-added transients. Variable temperature (VT) NMR spectra (150 to 360 K) were acquired for  $\text{MASnCl}_3$ ,  $\text{MASnBr}_3$  and  $\text{MASnI}_3$  using a Bruker NEO 500 spectrometer equipped with a Bruker Smart Variable Temperature (BSVT) unit. The heat exchanger source was liquid nitrogen with a dry nitrogen gas source for temperatures below 235 K or an ethanol/dry ice bath, with dry air as the VT gas for temperatures in the 235 K to room temperature range. The variable offset cumulative spectra (VOCS)<sup>45</sup> approach (3-4 steps with 50 kHz transmitter frequency steps) was used for the complete acquisition of the resulting spectra for  $\text{MASnCl}_3$ ,  $\text{MASnBr}_3$  and decomposing  $\text{MASnI}_3$ . The individual spectra were added using the skyline projection method. To ensure detection of by-products that may have longer spin-lattice relaxation times, recycle delays were set based on arrayed parameter optimizations. Tin-119 NMR spectra were referenced to tetramethylcyclohexyl tin ( $\delta_{\text{iso}} = -97.35$  ppm), a secondary reference with respect to  $\text{Sn}(\text{CH}_3)_4$  (0 ppm). Temperature calibrations were performed using  $\text{MAPbCl}_3$ , a method developed by this group.<sup>46</sup>

High-temperature  $^{119}\text{Sn}$  MAS NMR spectra were acquired on a wide-bore Bruker Avance III HD 400 MHz spectrometer equipped with a 7 mm double-resonance probe, spinning at 3.0 kHz. The sample was heated using a 50 W  $\text{CO}_2$  laser, and the temperature calibrated using the  $^{79}\text{Br}$  NMR signal of  $\text{KBr}$  as an external standard.<sup>47</sup> The room-temperature spectrum was acquired with a pulse length of  $4.6 \mu\text{s}$  ( $90^\circ$  tip angle), a recycle delay of 20 s, and 20480 coadded transients. At higher temperatures, recycle delays of 5 s ( $T = 453$  K) and 1 s ( $T = 533$  K) were used, with 8k and 4k transients, respectively. Tetramethyltin (25% in  $\text{CHCl}_3$ ) was used as the chemical shift reference (0 ppm).

Solid-state  $^{119}\text{Sn}$  NMR spectra were fit using the Maryland Convention,<sup>48,49</sup> proposed by Mason and Herzfeld,<sup>48</sup> and endorsed by IUPAC.<sup>50</sup> In this convention, three parameters are derived from the three principal components of the chemical shift tensor,  $\delta_{11}$ ,  $\delta_{22}$  and  $\delta_{33}$ :

$$\delta_{\text{iso}} = 1/3 (\delta_{11} + \delta_{22} + \delta_{33}) \quad (1)$$

$$\Omega = (\delta_{11} - \delta_{33}) \quad (2)$$

$$\kappa = 3 \frac{\delta_{22} - \delta_{\text{iso}}}{\Omega} \quad (3)$$

All  $^1\text{H}$ ,  $^{13}\text{C}$ , and  $^{207}\text{Pb}$  NMR experiments for  $\text{MAPbI}_3$  and  $\text{MASn}_{0.5}\text{Pb}_{0.5}\text{I}_3$  were performed at 7.05 T (300 MHz  $^1\text{H}$ ) on a Bruker Avance 300 NMR spectrometer using a double resonance ( $^1\text{H}/\text{X}$ ) NMR probe, where X was tuned to  $^{13}\text{C}$  ( $\omega_0/2\pi = 75.5$  MHz) and  $^{207}\text{Pb}$  ( $\omega_0/2\pi = 62.9$  MHz), respectively. All  $^1\text{H}$  experiments were performed with a MAS frequency of 12.0 kHz. A  $4.0 \mu\text{s}$   $\pi/2$  pulse ( $\gamma\text{B}_1/2\pi = 62.5$  kHz), 4 co-added transients and a recycle delay of 60 s were used for each measurement. All  $^1\text{H}$  NMR spectra were referenced by setting the  $^1\text{H}$  peak of adamantane to 1.85 ppm with respect to the primary reference sample, TMS with  $\delta(^1\text{H}) = 0.00$  ppm. All  $^{13}\text{C}$  experiments were performed under a MAS frequency of 5 kHz. A  $^1\text{H}$ - $^{13}\text{C}$  cross-polarization (CP)<sup>51</sup> technique with TPPM high-power  $^1\text{H}$  decoupling<sup>52</sup> ( $\gamma\text{B}_1/2\pi = 62.5$  kHz) and  $4.0 \mu\text{s}$   $\pi/2$  pulse ( $\gamma\text{B}_1/2\pi = 62.5$  kHz) for  $^1\text{H}$ , a contact time of 3.5 ms, and a recycle delay time of 60 s were used for each measurement. All  $^{13}\text{C}$  NMR spectra were referenced at 38.56 ppm for the high frequency  $^{13}\text{C}$  resonance of solid adamantane with respect to the primary standard sample, TMS at  $\delta(^{13}\text{C}) = 0.00$  ppm.<sup>53</sup> All  $^{207}\text{Pb}$  NMR spectra were collected under non-spinning sample conditions. A Hahn-echo ( $(\pi/2)_x-\tau_1-(\pi)_y-\tau_2$ -ACQ, where  $\tau_1$  and  $\tau_2$  represent the interpulse and refocusing delays, respectively)<sup>54</sup> was used, with 0.5 -5.0 s recycle delays. All  $^{207}\text{Pb}$  NMR spectra were referenced to the primary standard,  $\text{PbMe}_4$  with  $\delta(^{207}\text{Pb}) = 0.0$  ppm by setting the  $^{207}\text{Pb}$  peak of  $\text{MAPbCl}_3$  -647.5 ppm at 293(1) K.<sup>46</sup> All iodine-containing samples were synthesized and packed under  $\text{N}_2$  with initial analysis in either sealed tubes or under nitrogen gas. Decomposition studies were measured at room temperature under air, without controlling for humidity (over the course of 6 months the average humidity levels in Edmonton, Alberta were between 50 and 75%); at the 6 month mark a series of  $^{119}\text{Sn}$  NMR spectra were acquired using identical parameters, as discussed above, with the VOCS approach.

*Quantum chemical calculations:* Density functional theory (DFT) calculations on model tin-halide polyhedral anions,  $[\text{SnX}_6]^{4-}$  where X = Cl, Br and I, were carried out using the Amsterdam Density Functional (ADF) 2017 modeling suite.<sup>55-57</sup> The polyhedral structures were modeled using existing crystal structure data.<sup>10,21,58</sup> Relativistic effects were calculated using the zeroth order regular approximation (ZORA) method along with the ZORA/QZ4P basis set, which is optimized for relativistic calculations.<sup>59,60</sup> All calculations used the BP86 functional in the generalized gradient approximation (GGA).<sup>61,62</sup>

## RESULTS AND DISCUSSION

Variable temperature  $^{119}\text{Sn}$  NMR experiments were performed on a series of crystalline hybrid tin halide perovskites to gain electronic and structural insight through their magnetic shielding. Below we discuss the chemical shift range observed for the cubic crystalline parent hybrid tin perovskites and the impact on the  $^{119}\text{Sn}$  chemical shift anisotropy (CSA) as the phases change upon cooling. This is further expanded upon using quantum chemical calculations, as well as by examining the changes in  $^{119}\text{Sn}$  and  $^{207}\text{Pb}$  NMR spectra when mixing B-sites ( $\text{Sn}/\text{Pb} = 1/1$ ).

### Parent Materials – $\text{MASnX}_3$ ( $X = \text{Cl}, \text{Br}$ and $\text{I}$ )

PXRD patterns for the solvent-synthesized polycrystalline  $\text{MASnX}_3$  ( $X = \text{Cl}, \text{Br}$  and  $\text{I}$ ) samples are provided in Figure 1a at room temperature and agree with previously reported structures with  $\text{MASnCl}_3$  (space group  $\text{P1}$ ) material exhibiting a triclinic phase (vide infra) and,  $\text{MASnBr}_3$  and  $\text{MASnI}_3$  materials exhibiting a cubic phase (space group  $\text{Pm}\bar{3}\text{m}$ ) at room temperature. The  $^{119}\text{Sn}$  NMR spectra of  $\text{MASnX}_3$  ( $X = \text{Cl}, \text{Br}$  and  $\text{I}$ ) in their cubic ( $\text{Pm}\bar{3}\text{m}$ ) perovskite phases are shown in Figure 1b. The local  $\text{Sn(II)}$  chemical environment is coordinated to six halide anions forming  $[\text{SnX}_6]^{4-}$  octahedral clusters as shown in Figure 1c. As expected, the unit cell undergoes an expansion ( $a = 5.604 \text{ \AA}$  ( $\text{Cl}$ )  $\rightarrow 5.901 \text{ \AA}$  ( $\text{Br}$ )  $\rightarrow 6.204 \text{ \AA}$  ( $\text{I}$ )) to accommodate the increasing anionic radius ( $r(\text{Cl}^-) = 1.81 \text{ \AA}$ ,  $r(\text{Br}^-) = 1.96 \text{ \AA}$ , and  $r(\text{I}^-) = 2.20 \text{ \AA}$ ) proceeding down Group 17.<sup>43,63</sup>

With the Sn positioned at a cubic site of symmetry surrounded by six identical halide neighbors, the resulting lineshape for each parent phase is Gaussian-like in nature, with no evidence of chemical shift anisotropy at moderate magnetic field strengths. This is expected due to its spherical symmetry. For  $\text{MASnCl}_3$  in the cubic phase, the observed Gaussian lineshape is consistent with that expected from indirect spin-spin coupling between  $^{119}\text{Sn}$  and the six directly bonded  $^{35/37}\text{Cl}$  nuclei (i.e.,  $^1J(^{119}\text{Sn}, ^{35/37}\text{Cl})$ ; both  $^{35}\text{Cl}$  and  $^{37}\text{Cl}$  are  $I = 3/2$  nuclei). A first-order  $^{119}\text{Sn}$  NMR spectrum contains 19 overlapping peak multiplets (Figure S2a) due to  $^1J(^{119}\text{Sn}, ^{35}\text{Cl})$  and  $^1J(^{119}\text{Sn}, ^{37}\text{Cl})$ .<sup>64</sup> Although a splitting pattern to this interaction is not resolved, reported  $^1J(^{119}\text{Sn}, ^{35/37}\text{Cl})$  values ranging from 275 to 470 Hz are consistent with the observed linewidth for  $\text{MASnCl}_3$ .<sup>65</sup> However, the possible impact of the  $^{35/37}\text{Cl}$  nuclear quadrupole interactions on the  $^{119}\text{Sn}$  lineshapes cannot be discounted.<sup>31,66</sup> Likewise, indirect spin-spin interactions between  $^{119}\text{Sn}$  and  $^{79/81}\text{Br}$  (both  $I = 3/2$ ) and  $^{127}\text{I}$  ( $I = 5/2$ , see Fig. S2b for the predicted first-order splitting pattern in this case) surely play a role in the observed  $^{119}\text{Sn}$  lineshapes, but the much larger nuclear quadrupole interactions expected for these nuclei preclude a straightforward analysis. See Ref. 31 & 35 for a comparable analysis of  $^{207}\text{Pb}$ -halide spin-spin coupling in  $\text{MAPbX}_3$  perovskites. We note

that the  $\text{SnI}_6$  polyhedron in  $\text{MASnI}_3$  is not a perfect octahedron, as previously discussed<sup>10</sup>; DFT results (below) on this very small distortion suggests a very small CSA ( $\Omega < 10$  ppm) may be present. Each parent phase has a characteristic isotropic chemical shift ( $\delta_{\text{iso}}$ ) with  $\text{MASnCl}_3$  being the most shielded of the series,  $\delta_{\text{iso}} = -404$  (1) ppm;  $\text{MASnBr}_3$  is shifted slightly to higher frequency,  $\delta_{\text{iso}} = -315$  (1) ppm and  $\text{MASnI}_3$  is the most deshielded,  $\delta_{\text{iso}} = 155$  (2) ppm. Over this series the band gaps span approximately 2.5 eV: 3.69, 2.2 and 1.2 eV, respectively for  $\text{MASnCl}_3$  (monoclinic, thin film),  $\text{MASnBr}_3$  (cubic) and  $\text{MASnI}_3$  (cubic);  $\text{MASnCl}_3$  is white in color while  $\text{MASnI}_3$  has a metallic black appearance.<sup>10,19,43,67-69</sup>

The NMR chemical shift is sensitive to the electronic and local structure; therefore, with any change or disturbance about the local nuclear electronic environment, an associated change in the shielding will be detected. The shielding contributions of these semiconducting materials are impacted by the differing contributions of the diamagnetic and paramagnetic shielding components. In this case the material with the largest bandgap ( $\text{MASnCl}_3$ ) is located to lower frequency, experiencing a greater shielding whereas a gradual deshielding is observed as the halide octahedron is replaced by Br and again by I. The halide  $\text{MASnX}_3$  series spans nearly 550 ppm when in the cubic environment. A linear relationship between the optical bandgaps and the experimentally determined  $^{119}\text{Sn}$  isotropic chemical shifts appear to be present and may prove to be a practical analytical tool to describe solid solutions of these hybrid materials. The nuclear magnetic shielding is sensitive to the electronic structure about the nucleus of interest and thus is impacted by the local structure. Nuclei which have directly bonded halogen atoms usually exhibit either a normal halogen dependence (NHD), wherein the magnetic shielding increases with the mass of the halogen atom, or such as the  $^{119}\text{Sn}$  nuclei in this study, the inverse halogen dependence (IHD) wherein the magnetic shielding decreases with halide mass. These effects have been attributed to a spin-orbit contribution to the magnetic shielding.<sup>70</sup> In their computational study of Pb(II) and Pb(IV) halides, Dybowski and coworkers found that the spin-orbit contribution to shielding is essentially invariant to halide mass for the Pb(II) nuclei, but is responsible for the NHD for Pb(IV) nuclei. The IHD for the former was attributed to the paramagnetic contribution to magnetic shielding.<sup>71</sup> Table S2 summarizes the calculated paramagnetic ( $\sigma_{\text{para}}$ ), diamagnetic ( $\sigma_{\text{dia}}$ ) and spin-orbit ( $\sigma_{\text{so}}$ ) contributions to the Sn magnetic shielding for a series of  $[\text{SnX}_4]^{4-}$  model compounds. Qualitatively, the experimental trends are reproduced. In particular, the IHD is correctly predicted by these results. However, in contrast to the computational results reported by Dybowski and coworkers for Pb(II) halide complexes, our results suggest that the IHD observed for these Sn(II) complexes cannot be ascribed solely to the paramagnetic term:  $\sigma_{\text{para}}$  and  $\sigma_{\text{so}}$  contribute almost equally to the IHD. Both phenomena are impacted by numerous factors, such as structure and the local environment. A detailed study of this phenomenon requires an

examination of many more samples and thus is beyond the scope of the present study, but it is a promising avenue that merits future consideration.

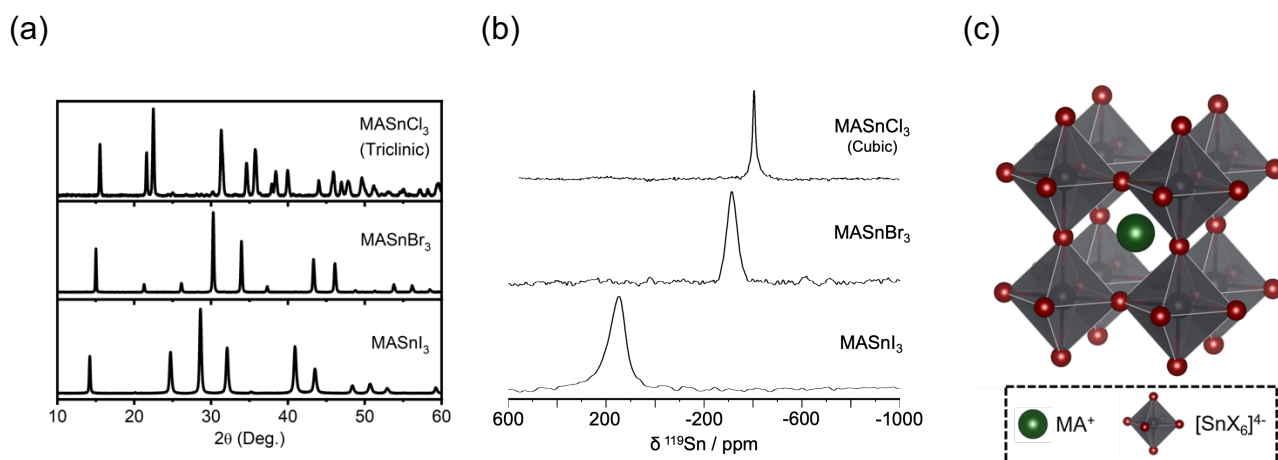


**Figure 1:** (a) Room temperature powder X-ray diffraction patterns for freshly synthesized MASnX<sub>3</sub> (X = Cl (Triclinic), Br (Cubic) and I (Cubic)). (b) Solid-state <sup>119</sup>Sn NMR spectra of cubic methylammonium tin halide perovskites, MASnX<sub>3</sub> where X= Cl, Br and I; MASnCl<sub>3</sub> ( $\omega_r/2\pi = 3$  kHz; 9.4 T;  $T_{\text{sample}} = 533$  (5) K), MASnBr<sub>3</sub> ( $\omega_r/2\pi = 10$  kHz; 7.05 T;  $T_{\text{sample}} = 290$  (1) K) and MASnI<sub>3</sub> (non-spinning; 7.05 T;  $T_{\text{sample}} = 290$  (1) K). (c) Graphic illustration of the arrangement of [SnX<sub>6</sub>]<sup>4-</sup> clusters.

### MASnCl<sub>3</sub>

Methylammonium tin chloride is a white crystalline material that exists in four unique crystallographic phases. Unlike its sister compound MAPbCl<sub>3</sub>, which is stable and resides in the cubic phase under ambient conditions, the Sn congener undergoes three phase changes between 300 and 478 K,<sup>31,43</sup> and only resides in a cubic (Pm-3m) crystal phase hexacoordinated to Cl with corner sharing polyhedra above 478 K. At ambient conditions (< 300 K) the crystal structure reverts to a triclinic (space group, P1) structure with Sn being five-coordinate in a distorted square pyramidal type polyhedron, with a zipper-like Sn-Cl-Sn-Cl-Sn chain structure running along the B axis. Slightly above ambient conditions Furukawa et al. have reported a complex phase change region where the triclinic structure transforms to a monoclinic (space group, Pc) structure at 318 K, followed quickly by the evolution of a rhombohedral (space group, R3m) structure at 350 K.<sup>21</sup> The authors describe this as a breakdown in the symmetric trans Cl-Sn-Cl bonds present above 480 K, whereby the pseudo-cubic phase begins to have an asymmetric Cl-Sn---Cl bond, becoming increasingly stretched (or deformed) as the temperature decreases.<sup>21,72</sup> Figure 2 shows the minor response in the CSA to these structural changes using variable-temperature <sup>119</sup>Sn NMR spectroscopy of MASnCl<sub>3</sub>. Beginning at 250 K, the MASnCl<sub>3</sub> sample is gradually heated through each phase transition temperature: triclinic ( $\Omega = 700$  (15) ppm;  $T = 245$  K) → monoclinic ( $\Omega = 643$  (15) ppm;  $T = 320$  K) → rhombohedral ( $\Omega = 620$  (10) ppm;  $T = 360$  K) → cubic ( $\Omega = 0$  ppm;  $T = 533$  K; full width

at half maximum, FWHM = 2.72 kHz). As the sample is heated towards the cubic phase transition temperature (533 K), the CSA powder pattern drastically decreases (Figure S3). The decrease in CSA appears to relate to this Cl-Sn---Cl distortion (e.g., Sn---Cl - 3.19 Å (triclinic) → 3.16 Å (monoclinic) → 3.03 Å (rhombohedral) → 2.88 Å (cubic)) about the Sn environment. These findings are further supported qualitatively by the DFT calculations, where the largest CSA is associated with the triclinic phase, although the experimentally observed span is underestimated by DFT. Table 1 summarizes the CSA parameters obtained from fitting both magic-angle spinning (MAS) and non-spinning  $^{119}\text{Sn}$  NMR spectra (Figure 2).

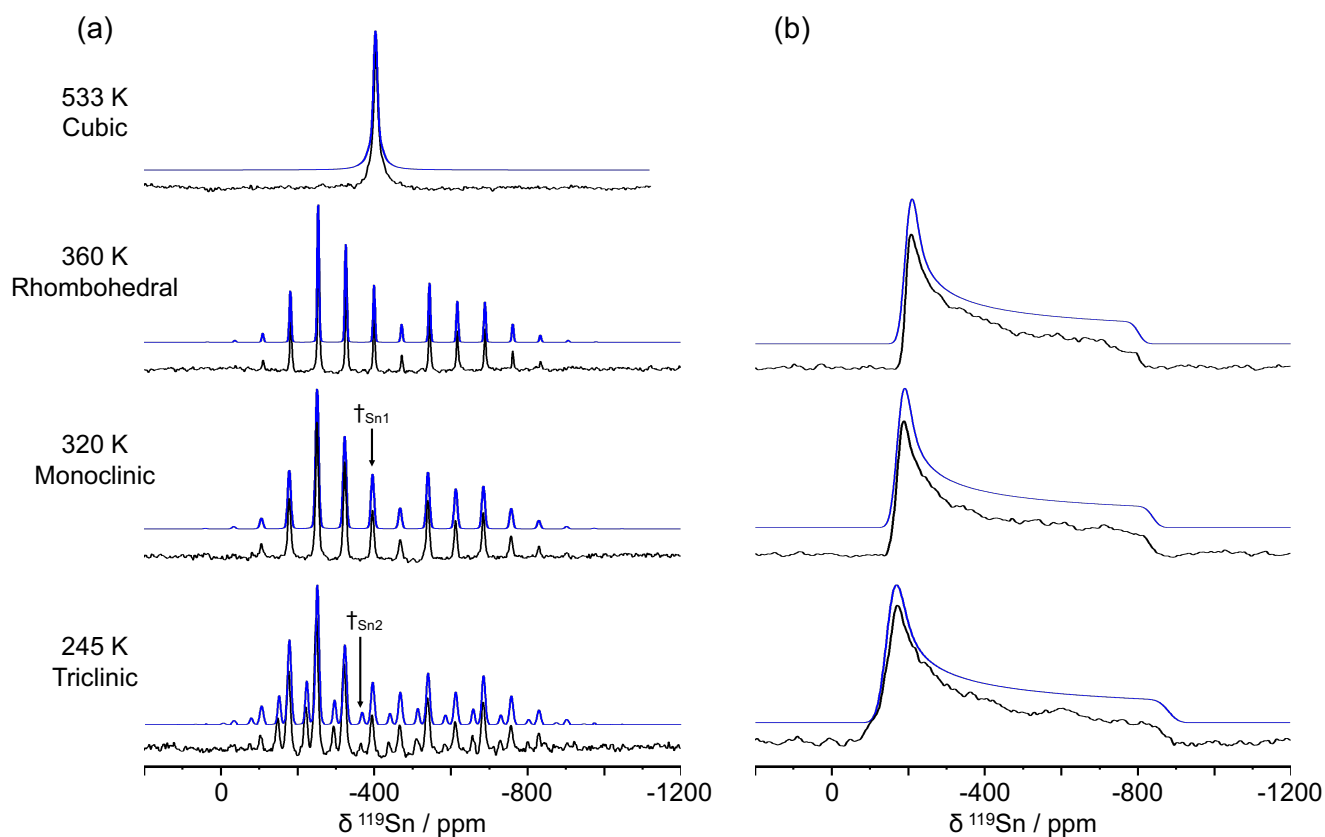


**Figure 2:** Experimental (black) and simulated (blue) variable temperature MAS (a) and non-spinning (b)  $^{119}\text{Sn}$  NMR spectra of  $\text{MASnCl}_3$  for cubic (a,  $T = 533\text{ K}$ ;  $B_0 = 9.4\text{ T}$ ;  $\omega_r/2\pi = 3\text{ kHz}$ ; 3202 co-added transients), rhombohedral (a,  $T = 360\text{ K}$ ;  $B_0 = 11.75\text{ T}$ ;  $\omega_r/2\pi = 13.5\text{ kHz}$ ; 488 co-added transients and b,  $T = 360\text{ K}$ ;  $B_0 = 11.75\text{ T}$ ; non-spinning; 256 co-added transients), Monoclinic (a,  $T = 320\text{ K}$ ;  $B_0 = 11.75\text{ T}$ ;  $\omega_r/2\pi = 13.5\text{ kHz}$ ; 512 co-added transients and b,  $T = 318\text{ K}$ ;  $B_0 = 11.75\text{ T}$ ; non-spinning; 256 co-added transients) and triclinic (a,  $T = 245\text{ K}$ ;  $B_0 = 11.75\text{ T}$ ;  $\omega_r/2\pi = 13.5\text{ kHz}$ ; 1024 co-added transients and b,  $T = 245\text{ K}$ ;  $B_0 = 11.75\text{ T}$ ; non-spinning; 1024 co-added transients) crystal structures. Note:  $\delta_{\text{iso}}$  is indicated as  $\dagger_{\text{Sn1}}$  with a second tin site at 245 K indicated by  $\dagger_{\text{Sn2}}$ .

### MASnBr<sub>3</sub>

The unique corner-sharing [BX<sub>6</sub>] octahedra in the high-temperature aristotype perovskite structure allows for a series of tilts (i.e., cooperative rotations) as the temperature decreases and can enter subsequent phases. As noted above, the high temperature  $\alpha$ -phase (space group, Pm3m) is cubic with Sn surrounded by six Br<sup>-</sup> neighbors forming perfect corner-sharing octahedra with the methylammonium cation sitting in the cuboctahedron site coordinated to 12 Br<sup>-</sup>.<sup>73</sup> The non-spinning <sup>119</sup>Sn NMR spectrum shows a single Gaussian-like peak, with a FWHM *ca.* 8.0 kHz and an isotropic chemical shift of -315 ppm (Figure 3). Onoda-Yamamuro et al. reported that the MASnBr<sub>3</sub> perovskite converts from a semi-conducting cubic solid to an insulator at 195 K with a rhombohedral crystal structure (R2c or R-3c) when using a deuterated MA cation.<sup>74</sup> A synchrotron study on non-deuterated MASnBr<sub>3</sub> (as studied herein) revealed that the only low temperature phase observed is orthorhombic (space group Pmc2<sub>1</sub>).<sup>58</sup> They further extensively studied the heating and cooling of this material between 188 and 230 K, but could not find evidence of this 3<sup>rd</sup> rhombohedral phase. The authors suggest this could be due to a strong deuterium isotope effect on the phase boundaries which has been previously reported in MAgGeCl<sub>3</sub>, where CD<sub>3</sub>ND<sub>3</sub>GeCl<sub>3</sub> is rhombohedral and CH<sub>3</sub>NH<sub>3</sub>GeCl<sub>3</sub> is cubic at a high temperature (349 K).<sup>9,58,75</sup> To determine the <sup>119</sup>Sn NMR parameters of the low-temperature MASnBr<sub>3</sub> orthorhombic phase, the sample was cooled to 200 K (Figure 3). The asymmetric <sup>119</sup>Sn lineshape ( $\delta_{\text{iso}} = -340$  ppm;  $\Omega = 790$  ppm) is consistent with an orthorhombic phase as the Sn center is no longer in the symmetric environment seen at higher temperatures. The large CSA determined experimentally is further supported by DFT calculations (vide infra, Table S1).

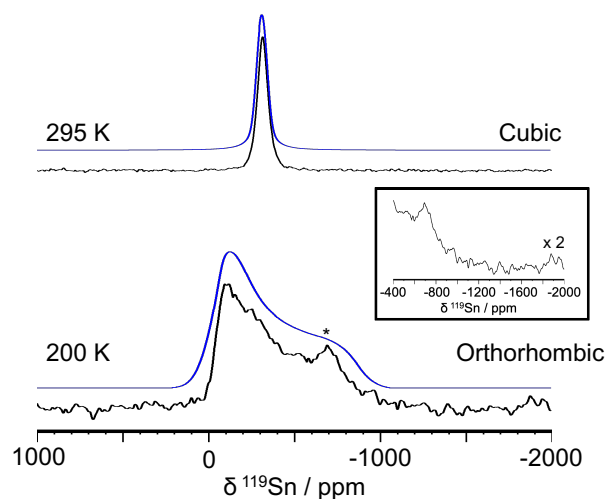


**Figure 3:** Experimental (black) and simulated (blue) variable temperature  $^{119}\text{Sn}$  NMR spectra of  $\text{MASnBr}_3$  (top) cubic ( $T = 295\text{ K}$ ;  $B_0 = 7.05\text{ T}$ ; non-spinning; 2048 co-added transients) and (bottom) orthorhombic ( $T = 200\text{ K}$ ;  $B_0 = 11.75\text{ T}$ ; non-spinning; 256 co-added transients). Note the presence of a  $\text{SnBr}_2$  impurity (\*, center-of-gravity shift  $\delta_{\text{cgs}} = -639\text{ ppm}$ ) is apparent in the spectrum acquired at 200 K; it is also present in the spectrum acquired at 295 K, but less apparent due to the different nuclear relaxation parameters as the sample is cooled and because, unlike  $\text{MASnBr}_3$ ,  $\text{SnBr}_2$  is not in a cubic environment at 295 K and thus its peak is not sharp. Inset is the orthorhombic spectrum vertically scaled by 2 to highlight the  $\text{SnBr}_2$  ( $\delta_{\text{cgs}} = -639\text{ ppm}$ ) impurity present, as well as the region where the potential degradation product,  $\text{MA}_2\text{SnBr}_6$ , would appear.

### $\text{MASnI}_3$

$\text{MASnI}_3$  is fascinating as, in addition to its attractive semiconducting properties with reported bandgaps of between 1.21 and 1.35 eV being in a suitable range for direct bandgap solar absorbing applications, the Cs and MA perovskites also display some metallic properties.<sup>10,76</sup> As observed for the  $\text{MASnBr}_3$  material,  $\text{MASnI}_3$  also can exist in two phases, with the  $\alpha$ - $\text{MASnI}_3$  being cubic (Pm-3m) and more recently reported as *pseudo* cubic (tetragonal with a space group of P4mm), while the low temperature (200 K)  $\beta$ - $\text{MASnI}_3$  phase is tetragonal (I4cm).<sup>10,43,73,77</sup> Figure 4 shows the non-spinning  $^{119}\text{Sn}$  NMR spectra for the  $\alpha$ - and  $\beta$ - $\text{MASnI}_3$  phases at 295 and 190 K, respectively; the  $^{119}\text{Sn}$  NMR spectrum for the  $\alpha$ -phase has a Gaussian-like lineshape (FWHM *ca.* 8.95 kHz) with  $\delta_{\text{iso}} = 155\text{ ppm}$ , consistent with the nearly cubic structure as reported by Stoumpos et al.<sup>10</sup> As described by these authors, a non-centrosymmetric tetragonal space group is the best description for the hybrid perovskite phase. Unlike a single atom (e.g.,  $\text{Cs}^+$ ) being able to occupy the 1b Wyckoff position at the center of the cuboctahedron, organic cations (e.g.,  $\text{CH}_3\text{NH}_3^+$  or  $\text{HC}(\text{NH}_2)_2^+$ ) cannot satisfy this condition, thereby creating structural disorder within the cage and the potential for hydrogen---halide interactions.

The  $^{119}\text{Sn}$  NMR spectrum for the  $\beta$ -phase displays a small shielding anisotropy of  $\Omega = 190(10)$  ppm ( $\kappa = 0.55$ ), indicating sensitivity to the polyhedron distortion upon cooling, and the chemical shift changes by 250 ppm, shifting to lower frequency at  $\delta_{\text{iso}} = -100$  (3) ppm. A small deformation in the axial Sn-I bonds occurs as the pseudo-cubic crystalline sample is cooled from 295 to 190 K, which causes one Sn-I bond to shrink (3.057 Å) and the other to lengthen (3.158 Å). This change is directed along the  $c$ -axis of the crystal lattice while the four Sn-I ionic bonds arranged in the equatorial square-planar geometry remain constant at 3.1324 Å. The DFT results (below) do predict this increase in shielding anisotropy (as it did for the Cl) but underestimate its magnitude and poorly reproduce the chemical shift even when relativistic effects are incorporated in the calculation. The poor agreement may be due to the impact of the different electronic properties of the two phases and that  $\text{MASnI}_3$  can display unique semi-conducting and metal properties which may impact the experimental results but are not accurately incorporated in the present quantum chemical computations on an isolated anionic “molecular” complex.

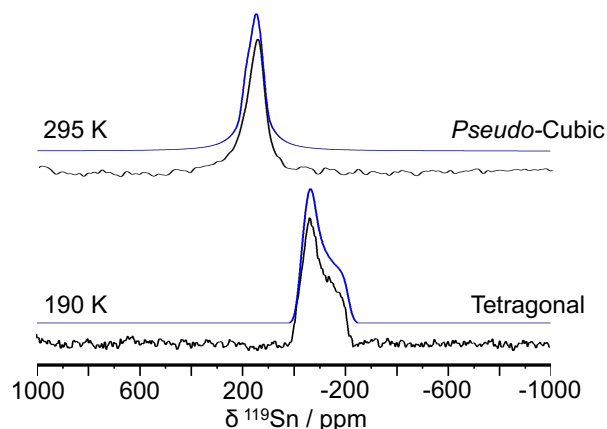


**Figure 4:** Experimental (black) and simulated (blue) variable temperature  $^{119}\text{Sn}$  NMR spectra of  $\text{MASnI}_3$  (top) pseudo-cubic ( $\alpha$ -phase,  $T = 295$  K;  $B_0 = 7.05$  T; non-spinning; 64 co-added transients) and (bottom) tetragonal ( $\beta$ -phase,  $T = 190$  K;  $B_0 = 11.75$  T; non-spinning; 4096 co-added transients).

**Table 1:** Experimental  $^{119}\text{Sn}$  NMR parameters for  $\text{MASnX}_3$ 

Compound	$\delta_{\text{iso}}$ (ppm)	Span, $\Omega$ (ppm)	Skew, $\kappa$	Space Group	Crystal System	Temperature (K)
$\text{MASnCl}_3$	-405 (1)	-	-	$Pm\bar{3}m$	Cubic	533
$\text{MASnCl}_3$	-400 (1)	620 (10)	0.95	$R3m$	Rhombohedral	350
$\text{MASnCl}_3$	-396 (1)	643 (15)	0.92	$Pc$	Monoclinic	318
$\text{MASnCl}_3 - \text{Sn1}$	-394(1)	700 (15)	0.97	$P1$	Triclinic	250
$\text{MASnCl}_3 - \text{Sn2}$	-367 (1)	710 (15)	1.0			
$\text{MASnBr}_3$	-315 (2)	-	-	$Pm3m$	Cubic	295
$\text{MASnBr}_3$	-340 (5)	800	1.0	$PmC21$	Orthorhombic	200
$\alpha\text{-MASnI}_3$	155 (2)	-	-	$P4mm$	Tetragonal	295
$\beta\text{-MASnI}_3$	-100 (3)	190 (6)	0.55	$I4cm$	Tetragonal	190

### Tracking $\text{MASnI}_3$ Degradation

Degradation of tin(II)-based perovskites has precluded the widespread application of these materials as an alternative to lead-halide perovskite materials. As such, many researchers continue to explore strategies to avoid rapid degradation under ambient conditions, such as encapsulation under an inert atmosphere, polymer coating or ion mixing (A-, B-, or X-sites). In order to investigate the ambient air stability and degradation of  $\text{MASnX}_3$  materials, we applied solid-state  $^{119}\text{Sn}$  NMR to study freshly synthesized  $\text{MASnX}_3$  samples; the summary of the results is presented below.

Under ambient conditions (i.e., room temperature, parafilm-sealed vial under air), degradation was not a significant concern when handling  $\text{MASnCl}_3$  and  $\text{MASnBr}_3$  compounds. In fact, based on the NMR spectra, there was no indication of degradation of  $\text{MASnCl}_3$  and  $\text{MASnBr}_3$  after two years from the date of synthesis. The only other material detected by  $^{119}\text{Sn}$  NMR in  $\text{MASnBr}_3$  was  $\text{SnBr}_2$ , which we believe is from unreacted starting material (vide supra). Previously, our group investigated the decomposition of  $\text{MAPbI}_3$  under hydro, thermal and hydrothermal exposure, revealing intricate spectral changes amongst  $\text{PbI}_2$ ,  $\text{MAPbI}_3$ ,  $\text{MAPbI}_3 \cdot \text{H}_2\text{O}$  and  $\text{MA}_4\text{PbI}_6 \cdot 2\text{H}_2\text{O}$ .<sup>12</sup> This approach is not feasible for  $\text{MASnI}_3$  as the compound shows the onset of degradation within an hour of synthesis; some evidence of degradation was also apparent when undertaking NMR studies of the low-temperature phase acquired under dry

nitrogen gas. Figure 5a shows a spectrum of the freshly synthesized material ( $\sim 30$  min post-synthesis under  $N_2$  atmosphere) which is denoted as time (T) = 0 h. As  $MASnI_3$  degrades, the linewidth and chemical shift change, with the latter shifting to a higher frequency over a period of hours as noted at T = 4 and 36 h (Figure 5a). The overall effect is quite drastic, with the spectral changes plotted in Figure 5b. Over a period of 30 hours the  $^{119}Sn$  NMR resonance broadens significantly from  $\sim 10$  kHz to  $>30$  kHz (Figure 5b). Degradation also leads to a shift of the resonance (center-of-gravity) to higher frequency by  $\sim 115$  ppm over the same period of time. The result of this reactivity can significantly skew the reported  $^{119}Sn$  NMR results, shifting the center-of-gravity upwards by a few 100 ppm and resulting in drastic changes to both the lineshape and breadth.

Although we cannot determine the exact decomposition product(s) in  $MASnI_3$  over this time frame, it is well documented that  $MASnI_3$  readily decomposes.<sup>78,79</sup> Some possible candidates include Sn(II)-based species such as SnO and  $SnI_2$ , or fully oxidized Sn(IV) species such as  $SnO_2$ ,  $SnI_4$  or  $MA_2SnI_6$ . During attempts to synthesize pure  $MASnI_3$ , a series of identifiable and unidentifiable compounds were observed in the PXRD. We were able to identify a few oxidized Sn(IV) species such as  $MA_2SnI_6$ ,  $SnO_2$  or  $SnI_4$ . Unfortunately, during this study we also determined that various commercial sources of  $SnI_2$  contains significant amounts of  $SnI_4$  (Figure S1). As a result, the presence of both Sn(II)- and Sn(IV)-based iodides may be observed in the PXRD due to unreacted impurities in the starting materials. Leading to further complications, the presence of  $SnI_4$  (or oxidation of  $SnI_2$ ) may further assist in forming  $MA_2SnI_6$ , while oxidation may occur during the PXRD measurement. The pure phase of  $MASnI_3$  reported in this work was examined immediately post-synthesis ( $\sim 30$  min) within a sealed capillary using pure ( $> 99\%$ )  $SnI_2$  as a starting material in tandem with the NMR study. The first 36-hour period after synthesis was continuously monitored using  $^{119}Sn$  NMR, however none of these degradation products were observed. The difficulty of using NMR to track decomposition is compounded by the fact that degradation products have different nuclear spin-lattice relaxation times (ranging from ms to sec) and suffer from varying degrees of chemical shift anisotropy, making it difficult to optimize acquisition parameters to observe all possible compounds uniformly, especially if the time-consuming VOCS approach is required to cover the large chemical shift range of nearly 13,000 ppm (covering Sn metal to  $MA_2SnI_6$ , spanning over 1 MHz at 7.05 T).<sup>38,41,80,81</sup> Interestingly, six months after the synthesis of the solution-prepared sample, a very broad  $^{119}Sn$  NMR signal spanning  $\sim 2800$  ppm (315 kHz FWHM) and centered at  $\sim 1500$  ppm was observed (Figure 5c). The aged  $MASnI_3$  appears to be trending towards the reported chemical shift range for Sn metal, indicating some type of intermediate phase(s) (Figure S4) that cannot be positively

identified but that resonates between the chemical shifts for metallic Sn and the  $\text{MASnI}_3$  parent phase (Figure 5d).<sup>80,81</sup>

While preparing this report, a publication appeared in which a sample of  $\text{MASnI}_3$  prepared using mechanochemical synthesis (MCS) exhibited a broad ( $\sim 100$  kHz,  $T_2^* = 10$   $\mu\text{s}$ ) and slightly asymmetric  $^{119}\text{Sn}$  NMR resonance with a reported isotropic chemical shift of 795 ppm.<sup>81</sup> This finding contrasts with the work reported here for a solution-based synthesis under  $\text{N}_2$ , where the non-spinning  $^{119}\text{Sn}$  NMR spectrum is Gaussian-like with a FWHM of *ca.* 9 kHz ( $T_2^* = 110$   $\mu\text{s}$ ) and with an isotropic chemical shift of 155 ppm. Similar differences are noted with the mixed bromide-iodide MCS sample in that report, where the  $^{119}\text{Sn}$  NMR resonance for  $\text{MASnBr}_{0.9}\text{I}_{2.1}$  ( $\delta = 1586$  ppm) is much broader and shifted to even higher frequency than that of their parent  $\text{MASnI}_3$  phase. The electronic properties of methylammonium tin halide perovskites would suggest that the NMR signal of a mixed Br/I phase would be located between their reported parent end members (i.e.,  $\text{MASnI}_3$  and  $\text{MASnBr}_3$ ), as observed in the case of the analogous MCS-made methylammonium lead halide perovskites, where all halide solid solutions are located between the parent end-members.<sup>28</sup> Likewise, these authors report the incorporation of  $\text{Cl}^-$  into the  $\text{MASnI}_3$  lattice, forming  $\text{MASnCl}_{2.7}\text{I}_{0.3}$ , based on the appearance of a new  $^{119}\text{Sn}$  NMR resonance centered at 249 ppm. This new resonance is situated between their reported parent end members ( $\text{MASnI}_3$ ,  $\delta = 795$  ppm and  $\text{MASnCl}_3$ ,  $\delta_{\text{iso}} = -395$  ppm), and is narrower than either of their reported  $\text{MASnI}_3$  or  $\text{MASnBr}_{0.9}\text{I}_{2.1}$  phases, all prepared using mechanochemical methods. Finally, Kubicki and coworkers detected metallic  $\beta$ -Sn as well as  $\text{MA}_2\text{SnI}_6$  and  $\text{SnO}_2$  in their MCS-made  $\text{MASnI}_3$  parent sample, achieved using longer acquisition times than attempted in our work.<sup>81</sup>

The  $^{119}\text{Sn}$  NMR results for the MCS-made  $\text{MASnI}_3$  ( $\delta = 795$  ppm),  $\text{MASnBr}_{0.9}\text{I}_{2.1}$  ( $\delta = 1586$  ppm) and  $\text{MASnCl}_{2.7}\text{I}_{0.3}$  ( $\delta = 249$  ppm) reported by Kubicki et al all appear at higher chemical shifts than the solution-synthesized  $\text{MASnI}_3$  phase presented in this work ( $\delta_{\text{iso}} = 155$  ppm). This difference may lie in structural variants produced by different synthetic methods, viz., MCS vs. solution. For example, we have shown using  $^{207}\text{Pb}$  NMR spectroscopy that MCS reduces resolution when compared to solution synthesis for the solid-solution  $\text{MAPbCl}_x\text{Br}_{3-x}$  perovskite series, as it reduces local and long-range ordering; however the chemical shifts and lineshape did not change significantly.<sup>28</sup> As  $\text{MASnI}_3$  and its mixed halides are complex materials, a more thorough investigation is needed to better understand the large changes in chemical shift and linewidth observed between MCS and solution synthesis, in addition to how the degradation of  $\text{MASnI}_3$ -based perovskites is impacted by both synthetic procedures and starting materials. The rapid degradation of  $\text{MASnI}_3$  observed in this work and the long acquisition times needed to identify the decomposition products may require complementary characterization techniques

to arrive at unambiguous conclusions for these complex materials and processes. The intuitive attractiveness of DNP to boost sensitivity and delay decomposition is undermined by the need to conduct such experiments at very low temperatures, which would induce further phase changes.<sup>84–86</sup>

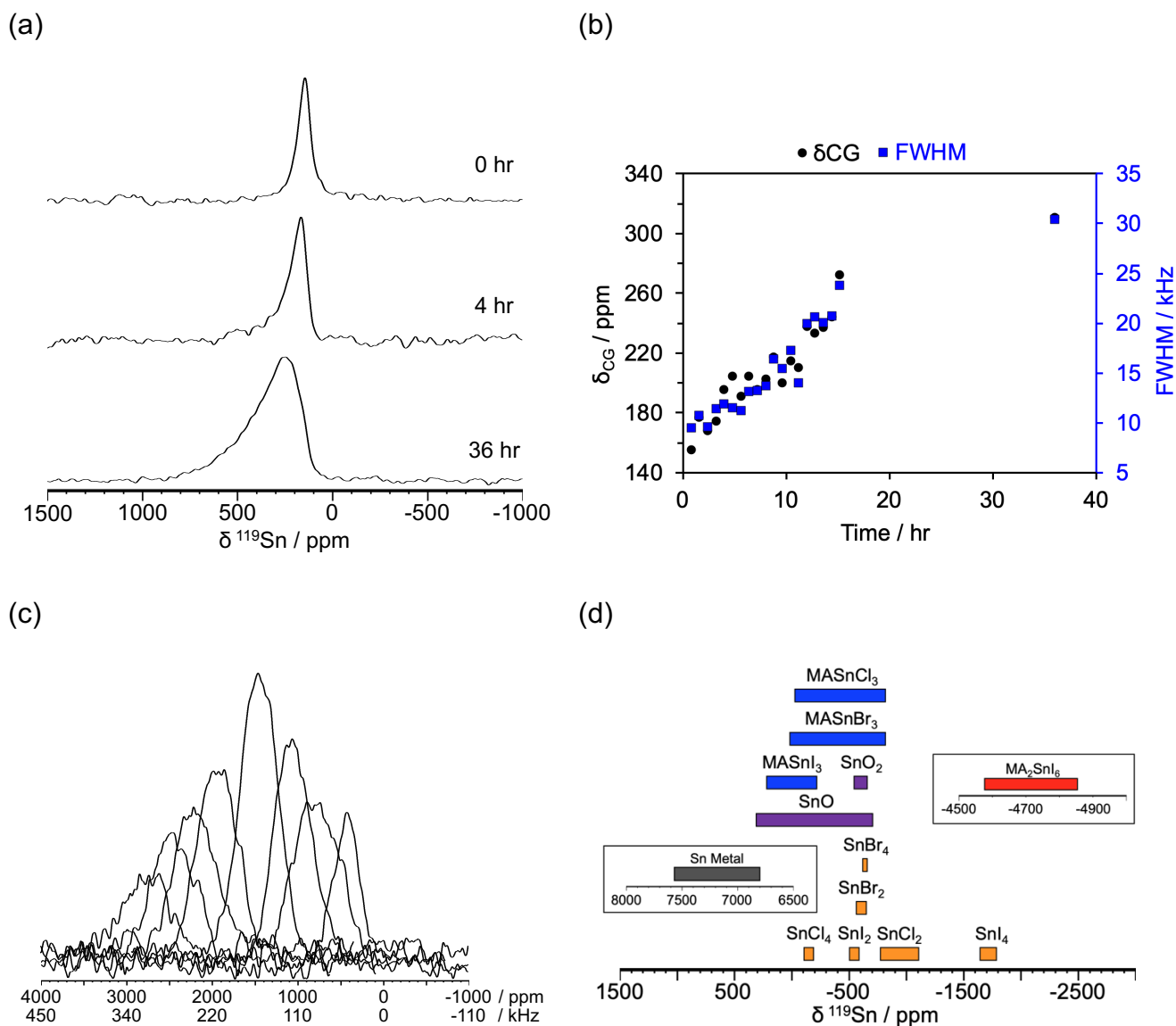


**Figure 5:** (a) Non-spinning  $^{119}\text{Sn}$  NMR spectra of  $\text{MASnI}_3$  of freshly synthesized (0 hr) to aged (36 hrs). (b) Changes in the center-of-gravity shift ( $\delta_{\text{CG}}$  / ppm) and full-width-half-maximum (FWHM / kHz) of  $\text{MASnI}_3$  with respect to time. (c) Non-spinning  $^{119}\text{Sn}$  NMR of  $\text{MASnI}_3$  after 6 months post-synthesis acquired using a VOCS approach. (d) Tin chemical shift scale for other tin halide and oxide compounds.

### Impact of X on $MASnX_3$ $^{119}Sn$ Magnetic Shielding

A quintessential NMR parameter to assess electronic and chemical structure is the isotropic chemical shift and its sensitivity to local structure. As the  $^{119}Sn$  NMR diamagnetic chemical shift range covers nearly 5,000 ppm depending on the chemical environment, this provides the ability to identify various tin halide species. The chemical shifts determined experimentally expand our understanding of the ranges that can potentially be observed for hybrid tin(II) halide perovskites. As seen for  $SnX_2$  salts (e.g.,  $SnCl_2$  in DMSO (-384 ppm) to I (-152 ppm)), the  $^{119}Sn$  in  $MASnCl_3$  is the most shielded ( $\delta_{iso} = -400$  ppm) with the Br and I phases gradually shifting to higher frequency, ranging over approximately 600 ppm. To assess the sensitivity to local structure, a series of  $[SnX_6]^{4-}$  anionic polyhedral clusters were assembled based on crystallographic data, and the Sn chemical shifts were calculated using ADF 2017 implementing a ZORA/QZ4P basis set to compare with experimental values. Figure 6a shows the relationship between the calculated magnetic shieldings and experimental chemical shifts for the eight unique phases studied here. The quantum chemical calculations using simple model compounds agree with the trends seen experimentally. To assess the sensitivity of the CSA to the structure of the local tin halide polyhedron, the distortion parameter ( $\lambda$ ) for each crystalline phase was determined from their crystal structures.<sup>87-89</sup> As shown in Figure 6b, the gradual change from a perfect Sn octahedron, in the cubic crystal lattice of  $MASnX_3$  (where X = Cl, Br or I), to the lower-symmetry tetragonal, orthorhombic, monoclinic and triclinic phases results in a sizable measured CSA which correlates with the distortion about the Sn center.

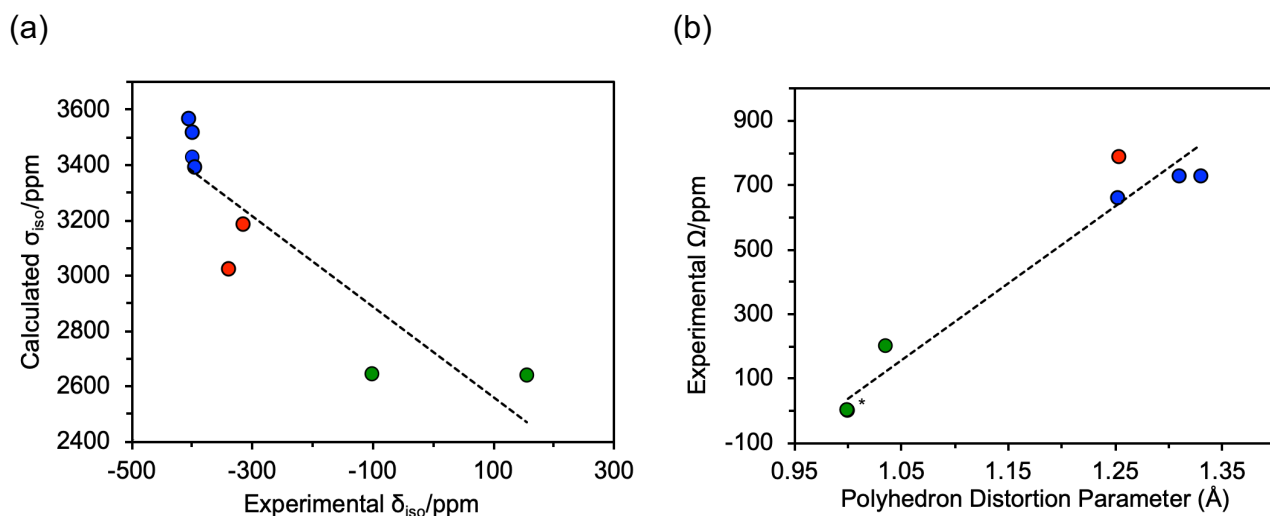


**Figure 6** (a) Calculated  $^{119}\text{Sn}$  magnetic shielding for tin halide polyhedron atomic clusters (blue =  $\text{MASnCl}_3$ , red =  $\text{MASnBr}_3$ , green =  $\text{MASnI}_3$ ) using a ZORA/QZ4P basis set as implemented in ADF 2017, and their relationship to experimental  $^{119}\text{Sn}$  chemical shifts. (b) Relationship between the experimental  $^{119}\text{Sn}$  chemical shift spans for methylammonium tin halide perovskites and their polyhedron distortion parameter calculated from known crystal structures. Note that all cubic structures of  $\text{MASnX}_3$  ( $X = \text{Cl, Br, I}$ ) have identical  $^{119}\text{Sn}$  CSAs and polyhedron distortion parameters (\*).

### *MASn<sub>0.5</sub>Pb<sub>0.5</sub>I<sub>3</sub> – Insight into Mixed B-site Alloyed Hybrid Perovskites*

Mixing the B-site between Sn and Pb has shown improved chemical stability for hybrid Sn(II)-containing perovskites while offering a further dimension to tune optical properties such as bandgap and emission.<sup>90–92</sup> Thus, expanding beyond our past research in mixed halides, we attempted to synthesize a mixed  $\text{Sn}^{2+}:\text{Pb}^{2+}$  analogue. Below we focus our discussion on a 1:1  $\text{Sn}^{2+}:\text{Pb}^{2+}$  mole ratio to form the  $\text{MASn}_{0.5}\text{Pb}_{0.5}\text{I}_3$  perovskite solid solution. PXRD shows that the  $\text{MAPbI}_3$  parent adopts a tetragonal phase, whereas the  $\text{MASnI}_3$  parent adopts a pseudo-cubic phase at room temperature.<sup>10</sup> As shown in Figure 7a, the PXRD data reveal that the  $\text{MASn}_{0.5}\text{Pb}_{0.5}\text{I}_3$  solid solution adopts the same pseudo-cubic structure as for the  $\text{MASnI}_3$  parent. We further performed room temperature  $^1\text{H}$ ,  $^{13}\text{C}$ ,  $^{119}\text{Sn}$  and  $^{207}\text{Pb}$  NMR spectroscopy to gain insight into the atomic-level changes both from the dynamic A-site cation ( $^1\text{H}$  and  $^{13}\text{C}$ ) and B-site cation ( $^{119}\text{Sn}$  and  $^{207}\text{Pb}$ ) perspectives upon  $\text{Sn}^{2+}/\text{Pb}^{2+}$  mixing.  $\text{MA}^+$  contains distinguishable hydrogens from the ammonium ( $\text{NH}_3$ ) and methyl ( $\text{CH}_3$ ) groups; the  $\delta_{\text{iso}}(^1\text{H})$  for the ammonium hydrogens appear to higher frequency than that for the methyl hydrogens. For example,  $\delta_{\text{iso}}(^1\text{H}) = 5.3$  and 2.4 ppm for  $\text{NH}_3$  and  $\text{CH}_3$  in  $\text{MASnI}_3$ , respectively (Figure 8a). Closer examination of  $^1\text{H}$  NMR spectra demonstrates a small but definite change in  $\delta_{\text{iso}}(^1\text{H})$  to higher frequency for both the

NH<sub>3</sub> and CH<sub>3</sub> hydrogens as Sn<sup>2+</sup> is replaced with Pb<sup>2+</sup> (Figure 8c). The small shoulder present in the <sup>1</sup>H NMR spectrum of MASnI<sub>3</sub> is likely assignable to degradation of the parent phase, as this spectrum was acquired between the 3<sup>rd</sup> and 4<sup>th</sup> hour decomposition points discussed above. The <sup>13</sup>C NMR chemical shift is also shifted to higher frequency and the linewidth narrows as Sn is replaced by Pb (Figures 8b and 8d). As past <sup>2</sup>H NMR experiments on deuterium-labeled MAPbI<sub>3</sub> demonstrated ultrafast MA<sup>+</sup> cation dynamics at room temperature,<sup>31,93</sup> the progressive changes in <sup>1</sup>H and <sup>13</sup>C NMR chemical shifts and linewidths are most likely due to changes in the unit cell volumes on going from MASnI<sub>3</sub> to MAPbI<sub>3</sub>:<sup>10</sup> the larger unit cell volume for MAPbI<sub>3</sub> implies a larger cuboctahedron space which allows faster MA<sup>+</sup> dynamics and hence a narrowing of the peaks in the <sup>1</sup>H and <sup>13</sup>C NMR spectra.

In contrast to the MA<sup>+</sup> cation, the B-site cations (i.e., Sn<sup>2+</sup> or Pb<sup>2+</sup>), are directly coordinated with six iodides to form [BI<sub>6</sub>]<sup>4-</sup> octahedra in the perovskite structure. The non-spinning <sup>207</sup>Pb NMR spectra for MAPbI<sub>3</sub> and MASn<sub>0.5</sub>Pb<sub>0.5</sub>I<sub>3</sub> (Figure 7) show Gaussian-like line shapes with a linewidth of *ca.* 27 and 28 kHz for MAPbI<sub>3</sub> and MASn<sub>0.5</sub>Pb<sub>0.5</sub>I<sub>3</sub>, respectively.  $\delta_{\text{iso}}(^{207}\text{Pb})$  is shifted towards higher frequency by *ca.* 130 ppm when Pb centered in MAPbI<sub>3</sub> is 50% replaced by Sn to form MASn<sub>0.5</sub>Pb<sub>0.5</sub>I<sub>3</sub>. Likewise, the non-spinning <sup>119</sup>Sn NMR spectra for both MASnI<sub>3</sub> and MASn<sub>0.5</sub>Pb<sub>0.5</sub>I<sub>3</sub> also give Gaussian-like broad line shapes with FWHM of *ca.* 9 and 18 kHz, respectively. However,  $\delta_{\text{iso}}(^{119}\text{Sn})$  for MASn<sub>0.5</sub>Pb<sub>0.5</sub>I<sub>3</sub> is shifted to lower frequency by  $\sim 70$  ppm. Neither the <sup>119</sup>Sn nor <sup>207</sup>Pb NMR spectra display any discernable spectral changes over several days (spectra were similar after two weeks in a sealed rotor), further supporting past findings by other researchers where Pb incorporation offsets degradation.<sup>90–92</sup> The NMR linewidths have been previously shown to be impacted by *T*<sub>2</sub>, direct and indirect spin-spin coupling between <sup>207</sup>Pb (or <sup>119</sup>Sn) and the six <sup>127</sup>I (*I* = 5/2; 100% abundant) nuclei in [BI<sub>6</sub>]<sup>4-</sup> octahedra.<sup>31,32</sup>

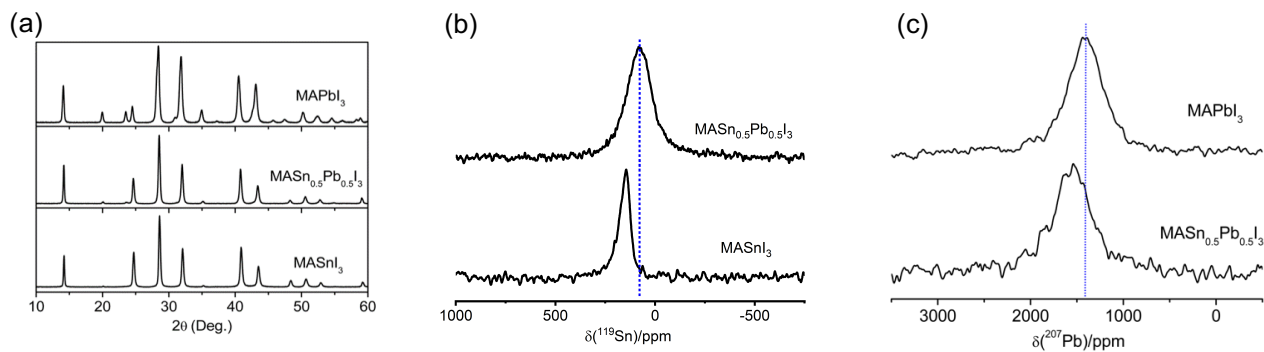


**Figure 7:** Experimentally determined room temperature PXRD (a) and solid-state <sup>119</sup>Sn (b) and <sup>207</sup>Pb (c) NMR spectra for freshly synthesized MASnI<sub>3</sub>, MASn<sub>0.5</sub>Pb<sub>0.5</sub>I<sub>3</sub> (nominal, EDX analyzed composition MASn<sub>0.42</sub>Pb<sub>0.58</sub>I<sub>3</sub>) and MAPbI<sub>3</sub> materials.

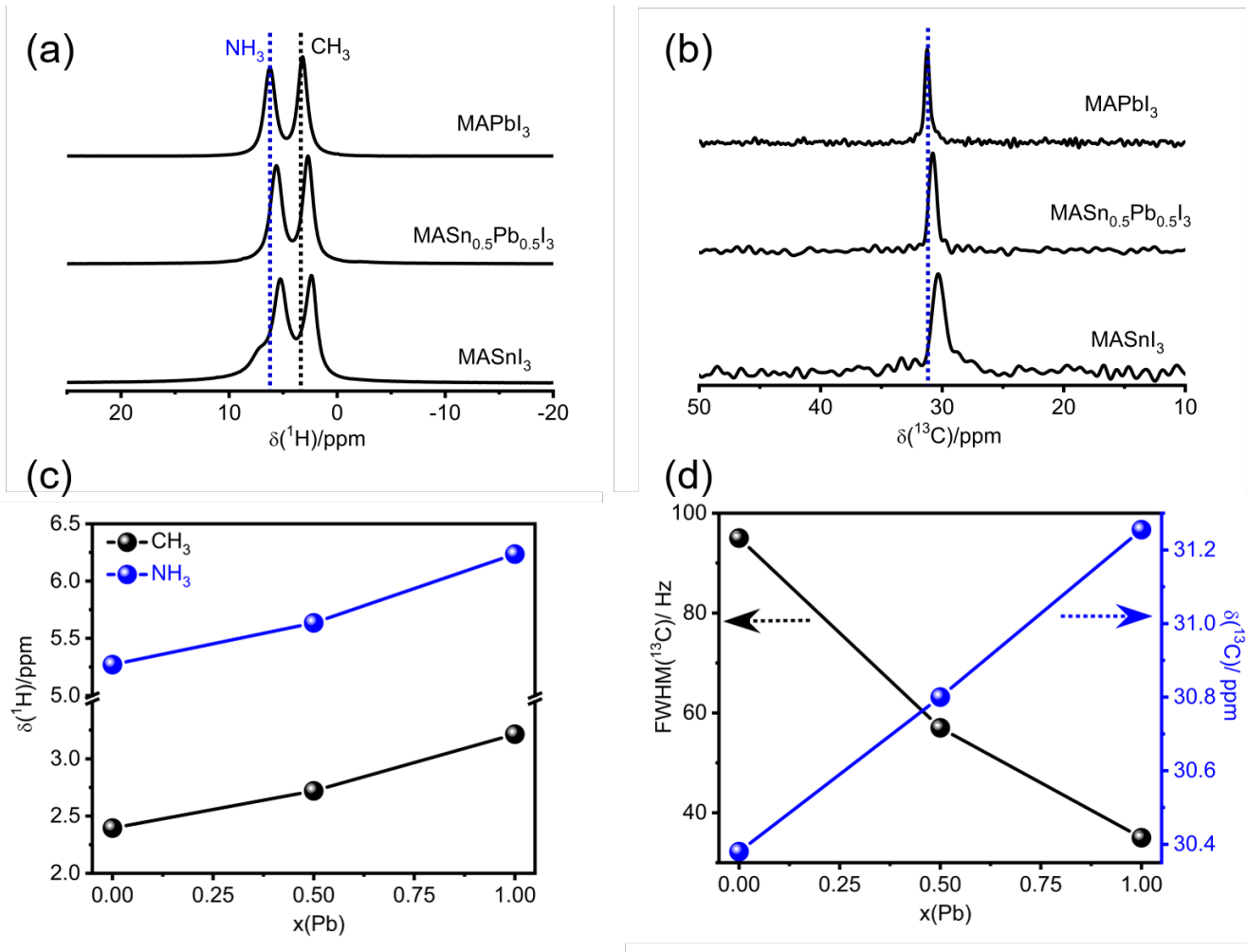


**Figure 8:** Room temperature <sup>1</sup>H (a, B<sub>0</sub> = 7.05 T and  $\omega_r/2\pi$  = 12 kHz) and <sup>13</sup>C (b, B<sub>0</sub> = 7.05 T and  $\omega_r/2\pi$  = 5 kHz) NMR spectra of freshly synthesized MASn<sub>1-x</sub>Pb<sub>x</sub>I<sub>3</sub> (x = 0, 0.5 and 1) materials. Change in <sup>1</sup>H chemical shifts for CH<sub>3</sub> and NH<sub>3</sub> units in MA<sup>+</sup> cation (c) and change in <sup>13</sup>C NMR chemical shifts (blue) and FWHM values (black) (d) for MASn<sub>1-x</sub>Pb<sub>x</sub>I<sub>3</sub> as a function with Pb concentration (x).

## CONCLUSIONS

In this work, we have discussed a series of hybrid methylammonium tin halide perovskites and their chemical shift ranges observed using  $^{119}\text{Sn}$  NMR spectroscopy and quantum chemical calculations. In each parent phase (where the Sn is positioned at a cubic site of symmetry), a distinct  $\delta_{\text{iso}}$  is determined with a characteristic shift to higher frequency ( $-404$  ppm to  $-315$  ppm to  $+155$  ppm for  $\text{MASnCl}_3$ ,  $\text{MASnBr}_3$  and  $\text{MASnI}_3$ , respectively) as the halide mass increases. This correlates with the changes in band gaps (a decrease of  $2.5$  eV from  $\text{MASnCl}_3$  to  $\text{MASnI}_3$ ), consistent with the fact that the NMR chemical shift is sensitive to changes in the paramagnetic shielding term and additional contributions from the spin orbit term of the local electronic environment. The relationship between changes in the local environment and the resulting chemical shifts is further explored via variable temperature  $^{119}\text{Sn}$  NMR spectroscopy: upon cooling, we see changes in the  $^{119}\text{Sn}$  CSA with phase changes. As  $\text{MASnI}_3$  is unstable, we performed an *in situ* NMR study over a course of 36 hours to track the changes in linewidths and chemical shifts with respect to time. Within hours, we observed an increase in linewidth and a  $\delta_{\text{CG}}$  shift to higher frequency; after 6 months a broad resonance spanning nearly 2800 ppm, trending towards Sn metal, appeared. This rapid degradation towards the metal may also help explain the dual semiconducting and metallic physical characteristics being reported for this system.<sup>10,72</sup> With the rapid degradation of  $\text{MASnI}_3$ , the discrepancies between our observed  $^{119}\text{Sn}$  NMR spectra of  $\text{MASnI}_3$  and those reported recently<sup>81</sup> may be due to the synthetic method used (solvent-based synthesis vs mechanochemical synthesis). In an attempt to improve the chemical stability of  $\text{MASnI}_3$ , we synthesized a mixed B-site ( $\text{Sn}^{2+}:\text{Pb}^{2+} = 1:1$  mole ratio) analogue and discovered that the  $\text{MASn}_{0.5}\text{Pb}_{0.5}\text{I}_3$  adopts a pseudo-cubic structure like the  $\text{MASnI}_3$  parent compound, and has  $^1\text{H}$ ,  $^{13}\text{C}$ ,  $^{119}\text{Sn}$  and  $^{207}\text{Pb}$  NMR spectral features that are distinct from those of the parent compounds, confirming its solid solution behavior. The incorporation of Pb appears to aid in resisting the degradation of these perovskites, whereby the mixed sample was easily handled and analyzed using both XRD and NMR spectroscopy without evidence of degradation over a two-week period. These findings provide an understanding of atomic-level structural property relationships in methylammonium tin halide perovskites and greater insight into the phase changes, material stability and  $\text{MASnI}_3$  decomposition that plague the use of tin(II) perovskites as a less toxic alternative to lead-based perovskites. Further research with mixed A, B or X-site analogues is required to reduce toxicity as one targets efforts to bridge the gap between efficient solar energy conversion and chemical stability to produce a new state-of-the-art solar absorbing material.

## **ASSOCIATED CONTENT**

### **SUPPORTING INFORMATION**

The Supporting Information is available free of charge on the ACS Publications website at DOI:

Calculated and experimental parameters (Tables S1-S3 & Figures S1-S4) are available in the Supporting Information (PDF).

### **AUTHOR INFORMATION**

\*Corresponding author: vladimir.michaelis@ualberta.ca

Note: The authors declare no competing financial interest.

### **ACKNOWLEDGEMENTS**

The Natural Sciences and Engineering Research Council (NSERC) of Canada (RGPIN-2016-05547), the Canada Foundation of Innovation, Future Energy Systems (CFREF), Alberta/Technical University of Munich International Graduate School for Hybrid Functional Materials (ATUMS, CREATE-463990-2015) and the University of Alberta are acknowledged for generous research support (V.K.M.). M.H. is supported by an NSERC PGS D3 and by an Alberta Innovates Graduate Scholarship. A. Karmakar is supported by the Alberta Innovates Graduate Scholarship. E.B. was partially supported by an Undergraduate Research Internship through the University of Alberta. S.K. is grateful to NSERC and CFI. A. Krishnamurthy is supported by a University of Manitoba Graduate Fellowship. The authors thank Prof. R.E. Wasylshen, Dr. A. Faucher, Ms. A. Geisler, Ms. R. Moore and Ms. S. Saggu for scientific discussions.

## REFERENCES

- (1) National Renewable Energy Laboratory (NREL). Best Research-Cell Efficiency Chart. <https://www.nrel.gov/pv/assets/pdfs/best-research-cell-efficiencies.20190923.pdf>.
- (2) Tennyson, E. M.; Doherty, T. A. S.; Stranks, S. D. Heterogeneity at Multiple Length Scales in Halide Perovskite Semiconductors. *Nat. Rev. Mater.* **2019**, *4*, 573–587.
- (3) Wei, H.; Huang, J. Halide Lead Perovskites for Ionizing Radiation Detection. *Nat. Commun.* **2019**, *10*, 1066.
- (4) Fu, Y.; Zhu, H.; Chen, J.; Hautzinger, M. P.; Zhu, X.-Y.; Jin, S. Metal Halide Perovskite Nanostructures for Optoelectronic Applications and the Study of Physical Properties. *Nat. Rev. Mater.* **2019**, *4*, 169–188.
- (5) Gao, P.; Bin Mohd Yusoff, A. R.; Nazeeruddin, M. K. Dimensionality Engineering of Hybrid Halide Perovskite Light Absorbers. *Nat. Commun.* **2018**, *9*, 5028.
- (6) Sum, T.-C.; Mathews, N. *Halide Perovskites: Photovoltaics, Light Emitting Devices, and Beyond*; Wiley-VCH: Weinheim, 2019.
- (7) Jung, H. S.; Park, N.-G. Perovskite Solar Cells: From Materials to Devices. *Small* **2015**, *11*, 10–25.
- (8) Borriello, I.; Cantele, G.; Ninno, D. Ab Initio Investigation of Hybrid Organic-Inorganic Perovskites Based on Tin Halides. *Phys. Rev. B* **2008**, *77*, 235214.
- (9) Yamada, K.; Mikawa, K.; Okuda, T.; Knight, K. S. Static and Dynamic Structures of  $\text{CD}_3\text{ND}_3\text{GeCl}_3$  Studied by TOF High Resolution Neutron Powder Diffraction and Solid State NMR. *J. Chem. Soc. Dalton Trans.* **2002**, (10), 2112–2118.
- (10) Stoumpos, C. C.; Malliakas, C. D.; Kanatzidis, M. G. Semiconducting Tin and Lead Iodide Perovskites with Organic Cations: Phase Transitions, High Mobilities, and Near-Infrared Photoluminescent Properties. *Inorg. Chem.* **2013**, *52*, 9019–9038.
- (11) Breternitz, J.; Schorr, S. What Defines a Perovskite? *Adv. Energy Mater.* **2018**, *8*, 1802366.
- (12) Askar, A. M.; Bernard, G. M.; Wiltshire, B.; Shankar, K.; Michaelis, V. K. Multinuclear Magnetic Resonance Tracking of Hydro, Thermal, and Hydrothermal Decomposition of  $\text{CH}_3\text{NH}_3\text{PbI}_3$ . *J. Phys. Chem. C* **2017**, *121*, 1013–1024.
- (13) Wang, D.; Wright, M.; Elumalai, N. K.; Uddin, A. Stability of Perovskite Solar Cells. *Sol. Energy Mater. Sol. Cells* **2016**, *147*, 255–275.
- (14) Juarez-Perez, E. J.; Ono, L. K.; Maeda, M.; Jiang, Y.; Hawash, Z.; Qi, Y. Photodecomposition and Thermal Decomposition in Methylammonium Halide Lead Perovskites and Inferred Design Principles to Increase Photovoltaic Device Stability. *J. Mater. Chem. A* **2018**, *6*, 9604–9612.

- (15) Li, J.; Cao, H.-L.; Jiao, W.-B.; Wang, Q.; Wei, M.; Cantone, I.; Lü, J.; Abate, A. Biological Impact of Lead from Halide Perovskites Reveals the Risk of Introducing a Safe Threshold. *Nat. Commun.* **2020**, *11*, 310.
- (16) Hu, H.; Dong, B.; Zhang, W. Low-Toxic Metal Halide Perovskites: Opportunities and Future Challenges. *J. Mater. Chem. A* **2017**, *5*, 11436–11449.
- (17) Feng, J.; Xiao, B. Effective Masses and Electronic and Optical Properties of Nontoxic  $\text{MASnX}_3$  (X = Cl, Br, and I) Perovskite Structures as Solar Cell Absorber: A Theoretical Study Using HSE06. *J. Phys. Chem. C* **2014**, *118*, 19655–19660.
- (18) Hong, Z.; Tan, D.; John, R. A.; Tay, Y. K. E.; Ho, Y. K. T.; Zhao, X.; Sum, T. C.; Mathews, N.; García, F.; Soo, H. Sen. Completely Solvent-Free Protocols to Access Phase-Pure, Metastable Metal Halide Perovskites and Functional Photodetectors from the Precursor Salts. *iScience* **2019**, *16*, 312–325.
- (19) Chiarella, F.; Zappettini, A.; Licci, F.; Borriello, I.; Cantele, G.; Ninno, D.; Cassinese, A.; Vaglio, R. Combined Experimental and Theoretical Investigation of Optical, Structural, and Electronic Properties of  $\text{CH}_3\text{NH}_3\text{SnX}_3$  Thin Films (X = Cl, Br). *Phys. Rev. B* **2008**, *77*, 045129.
- (20) Lang, L.; Yang, J.-H.; Liu, H.-R.; Xiang, H. J.; Gong, X. G. First-Principles Study on the Electronic and Optical Properties of Cubic  $\text{ABX}_3$  Halide Perovskites. *Phys. Lett. A* **2014**, *378*, 290–293.
- (21) Yamada, K.; Kuranaga, Y.; Ueda, K.; Goto, S.; Okuda, T.; Furukawa, Y. Phase Transition and Electric Conductivity of  $\text{ASnCl}_3$  (A = Cs and  $\text{CH}_3\text{NH}_3$ ). *Bull. Chem. Soc. Jpn.* **1998**, *71*, 127–134.
- (22) Yamada, K.; Nose, S.; Umehara, T.; Okuda, T.; Ichiba, S.  $^{81}\text{Br}$  NQR and  $^{119}\text{Sn}$  Mössbauer Study for  $\text{MSnBr}_3$  (M=Cs and  $\text{CH}_3\text{NH}_3$ ). *Bull. Chem. Soc. Jpn.* **1988**, *61*, 4265–4268.
- (23) Peedikakkandy, L.; Bhargava, P. Composition Dependent Optical, Structural and Photoluminescence Characteristics of Cesium Tin Halide Perovskites. *RSC Adv.* **2016**, *6*, 19857–19860.
- (24) Kumar, M. H.; Dharani, S.; Leong, W. L.; Boix, P. P.; Prabhakar, R. R.; Baikie, T.; Shi, C.; Ding, H.; Ramesh, R.; Asta, M.; et al. Lead-Free Halide Perovskite Solar Cells with High Photocurrents Realized Through Vacancy Modulation. *Adv. Mater.* **2014**, *26*, 7122–7127.
- (25) Ogomi, Y.; Morita, A.; Tsukamoto, S.; Saitho, T.; Fujikawa, N.; Shen, Q.; Toyoda, T.; Yoshino, K.; Pandey, S. S.; Ma, T.; et al.  $\text{CH}_3\text{NH}_3\text{Sn}_x\text{Pb}_{(1-x)}\text{I}_3$  Perovskite Solar Cells Covering up to 1060 nm. *J. Phys. Chem. Lett.* **2014**, *5*, 1004–1011.
- (26) Hao, F.; Stoumpos, C. C.; Cao, D. H.; Chang, R. P. H.; Kanatzidis, M. G. Lead-Free Solid-State Organic–Inorganic Halide Perovskite Solar Cells. *Nat. Photonics* **2014**, *8*, 489–494.
- (27) Noel, N. K.; Stranks, S. D.; Abate, A.; Wehrenfennig, C.; Guarnera, S.; Haghighirad, A.-A.; Sadhanala, A.; Eperon, G. E.; Pathak, S. K.; Johnston, M. B.; et al. Lead-Free Organic–Inorganic Tin Halide

Perovskites for Photovoltaic Applications. *Energy Environ. Sci.* **2014**, *7*, 3061–3068.

- (28) Karmakar, A.; Askar, A. M.; Bernard, G. M.; Terskikh, V. V.; Ha, M.; Patel, S.; Shankar, K.; Michaelis, V. K. Mechanochemical Synthesis of Methylammonium Lead Mixed-Halide Perovskites: Unraveling the Solid-Solution Behavior Using Solid-State NMR. *Chem. Mater.* **2018**, *30*, 2309–2321.
- (29) Karmakar, A.; Dodd, M. S.; Zhang, X.; Oakley, M. S.; Klobukowski, M.; Michaelis, V. K. Mechanochemical Synthesis of 3D and 0D Cesium Lead Mixed Halide Perovskite Solid Solutions. *Chem. Commun.* **2019**, *55*, 5079–5082.
- (30) Franssen, W. M. J.; van Es, S. G. D.; Dervişoğlu, R.; de Wijs, G. A.; Kentgens, A. P. M. Symmetry, Dynamics, and Defects in Methylammonium Lead Halide Perovskites. *J. Phys. Chem. Lett.* **2017**, *8*, 61–66.
- (31) Bernard, G. M.; Wasylishen, R. E.; Ratcliffe, C. I.; Terskikh, V.; Wu, Q.; Buriak, J. M.; Hauger, T. Methylammonium Cation Dynamics in Methylammonium Lead Halide Perovskites: A Solid-State NMR Perspective. *J. Phys. Chem. A* **2018**, *122*, 1560–1573.
- (32) Senocrate, A.; Moudrakovski, I.; Kim, G. Y.; Yang, T.; Gregori, G.; Grätzel, M.; Maier, J. The Nature of Ion Conduction in Methylammonium Lead Iodide: A Multimethod Approach. *Angew. Chemie Int. Ed.* **2017**, *56*, 7755–7759.
- (33) Kubicki, D. J.; Prochowicz, D.; Hofstetter, A.; Péchy, P.; Zakeeruddin, S. M.; Grätzel, M.; Emsley, L. Cation Dynamics in Mixed-Cation (MA)<sub>x</sub>(FA)<sub>1-x</sub>PbI<sub>3</sub> Hybrid Perovskites from Solid-State NMR. *J. Am. Chem. Soc.* **2017**, *139*, 10055–10061.
- (34) Kubicki, D. J.; Prochowicz, D.; Hofstetter, A.; Zakeeruddin, S. M.; Grätzel, M.; Emsley, L. Phase Segregation in Potassium-Doped Lead Halide Perovskites from <sup>39</sup>K Solid-State NMR at 21.1 T. *J. Am. Chem. Soc.* **2018**, *140*, 7232–7238.
- (35) Aebli, M.; Piveteau, L.; Nazarenko, O.; Benin, B. M.; Krieg, F.; Verel, R.; Kovalenko, M. V. Lead-Halide Scalar Couplings in <sup>207</sup>Pb NMR of APbX<sub>3</sub> Perovskites (A = Cs, Methylammonium, Formamidinium; X = Cl, Br, I). *Sci. Rep.* **2020**, *10*, 8229.
- (36) Harris, R. K.; Becker, E. D. NMR Nomenclature: Nuclear Spin Properties and Conventions for Chemical Shifts—IUPAC Recommendations. *J. Magn. Reson.* **2002**, *156*, 323–326.
- (37) Mundus, C.; Taillades, G.; Pradel, A.; Ribes, M. A <sup>119</sup>Sn Solid-State Nuclear Magnetic Resonance Study of Crystalline Tin Sulphides. *Solid State Nucl. Magn. Reson.* **1996**, *7*, 141–146.
- (38) Eichler, B. E.; Phillips, B. L.; Power, P. P.; Augustine, M. P. Solid-State and High-Resolution Liquid <sup>119</sup>Sn NMR Spectroscopy of Some Monomeric, Two-Coordinate Low-Valent Tin Compounds: Very Large Chemical Shift Anisotropies. *Inorg. Chem.* **2000**, *39*, 5450–5453.

- (39) Harris, R. K.; Sebal, A. High-Resolution Solid-State  $^{119}\text{Sn}$  And  $^{207}\text{Pb}$  NMR Study of Organotin and Organolead Chalcogenides: Observation Of J-Coupling in Solids. *Magn. Reson. Chem.* **1989**, *27*, 81–87.
- (40) Grey, C. P.; Cheetham, A. K.; Dobson, C. M. Temperature-Dependent Solid-State  $^{119}\text{Sn}$ -MAS NMR of  $\text{Nd}_2\text{Sn}_2\text{O}_7$ ,  $\text{Sm}_2\text{Sn}_2\text{O}_7$ , and  $\text{Y}_{1.8}\text{Sm}_{0.2}\text{Sn}_2\text{O}_7$ . Three Sensitive Chemical-Shift Thermometers. *J. Magn. Reson. Ser. A* **1993**, *101*, 299–306.
- (41) MacKenzie, K.; Smith, M. E. *Multinuclear Solid-State Nuclear Magnetic Resonance of Inorganic Materials, Volume 6*; Pergamon, 2002.
- (42) Gunther, W. R.; Michaelis, V. K.; Caporini, M. A.; Griffin, R. G.; Román-Leshkov, Y. Dynamic Nuclear Polarization NMR Enables the Analysis of Sn-Beta Zeolite Prepared with Natural Abundance  $^{119}\text{Sn}$  Precursors. *J. Am. Chem. Soc.* **2014**, *136*, 6219–6222.
- (43) Yamada, K.; Nakada, K.; Takeuchi, Y.; Nawa, K.; Yohei Yamane. Tunable Perovskite Semiconductor  $\text{CH}_3\text{NH}_3\text{SnX}_3$  (X: Cl, Br, or I) Characterized by X-Ray and DTA. *Bull. Chem. Soc. Jpn.* **2011**, *84*, 926–932.
- (44) Onoda-Yamamuro, N.; Matsuo, T.; Suga, H. Thermal, Electric, and Dielectric Properties of  $\text{CH}_3\text{NH}_3\text{SnBr}_3$  at Low Temperatures. *J. Chem. Thermodyn.* **1991**, *23*, 987–999.
- (45) Bureau, B.; Silly, G.; Buzaré, J. .; Legein, C.; Massiot, D. From Crystalline to Glassy Gallium Fluoride Materials: An NMR Study of and Quadrupolar Nuclei. *Solid State Nucl. Magn. Reson.* **1999**, *14*, 181–190.
- (46) Bernard, G. M.; Goyal, A.; Miskolzie, M.; McKay, R.; Wu, Q.; Wasylishen, R. E.; Michaelis, V. K. Methylammonium Lead Chloride: A Sensitive Sample for an Accurate NMR Thermometer. *J. Magn. Reson.* **2017**, *283*, 14–21.
- (47) Thurber, K. R.; Tycko, R. Measurement of Sample Temperatures under Magic-Angle Spinning from the Chemical Shift and Spin-Lattice Relaxation Rate of  $^{79}\text{Br}$  in KBr Powder. *J. Magn. Reson.* **2009**, *196*, 84–87.
- (48) Mason, J. Conventions for the Reporting of Nuclear Magnetic Shielding (or Shift) Tensors Suggested by Participants in the NATO ARW on NMR Shielding Constants at the University of Maryland, College Park, July 1992. *Solid State Nucl. Magn. Reson.* **1993**, *2*, 285–288.
- (49) Herzfeld, J.; Berger, A. E. Sideband Intensities in NMR-Spectra of Samples Spinning at the Magic Angle. *J. Chem. Phys.* **1980**, *73*, 6021–6030.
- (50) Harris, R. K.; Becker, E. D.; De Menezes, S. M. C.; Granger, P.; Hoffman, R. E.; Zilm, K. W. Further Conventions for NMR Shielding and Chemical Shifts (IUPAC Recommendations 2008). *Pure Appl. Chem.* **2008**, *80*, 59–84.

- (51) Pines, A.; Gibby, M. G.; Waugh, J. S. Proton-Enhanced Nuclear Induction Spectroscopy. A Method for High Resolution NMR of Dilute Spins in Solids. *J. Chem. Phys.* **1972**, *56*, 1776–1777.
- (52) Bennett, A. E.; Rienstra, C. M.; Auger, M.; Lakshmi, K. V.; Griffin, R. G. Heteronuclear Decoupling in Rotating Solids. *J. Chem. Phys.* **1995**, *103*, 6951–6958.
- (53) Earl, W. L.; Vanderbart, D. L. Measurement of  $^{13}\text{C}$  Chemical Shifts in Solids. *J. Magn. Reson.* **1982**, *48* (1), 35–54.
- (54) Hahn, E. L. Spin Echoes. *Phys. Rev.* **1950**, *80*, 580–594.
- (55) Te Velde, G.; Bickelhaupt, F. M.; Baerends, E. J.; Fonseca Guerra, C.; van Gisbergen, S. J. A.; Snijders, J. G.; Ziegler, T. Chemistry with ADF. *J. Comput. Chem.* **2001**, *22*, 931–967.
- (56) ADF 2019.3, SCM, Theoretical Chemistry, Vrije Universiteit, Amsterdam, The Netherlands.
- (57) Fonseca Guerra, C.; Snijders, J. G.; te Velde, G.; Baerends, E. J. Towards an Order-N DFT Method. *Theor. Chem. Accounts* **1998**, *99*, 391–403.
- (58) Swainson, I.; Chi, L.; Her, J.-H.; Cranswick, L.; Stephens, P.; Winkler, B.; Wilson, D. J.; Milman, V. Orientational Ordering, Tilting and Lone-Pair Activity in the Perovskite Methylammonium Tin Bromide,  $\text{CH}_3\text{NH}_3\text{SnBr}_3$ . *Acta Crystallogr. Sect. B Struct. Sci.* **2010**, *66*, 422–429.
- (59) Schreckenbach, G.; Ziegler, T. Calculation of NMR Shielding Tensors Using Gauge-Including Atomic Orbitals and Modern Density Functional Theory. *J. Phys. Chem.* **1995**, *99*, 606–611.
- (60) van Lenthe, E.; Ehlers, A.; Baerends, E.-J. Geometry Optimizations in the Zero Order Regular Approximation for Relativistic Effects. *J. Chem. Phys.* **1999**, *110*, 8943–8953.
- (61) Becke, A. D. Density-Functional Exchange-Energy Approximation with Correct Asymptotic Behavior. *Phys. Rev. A* **1988**, *38*, 3098–3100.
- (62) Perdew, J. P.; Yue, W. Accurate and Simple Density Functional for the Electronic Exchange Energy: Generalized Gradient Approximation. *Phys. Rev. B* **1986**, *33*, 8800–8802.
- (63) Shannon, R. D. Revised Effective Ionic Radii and Systematic Studies of Interatomic Distances in Halides and Chalcogenides. *Acta Cryst.* **1976**, *A32*, 751–767.
- (64) Lash, T. D.; Lash, S. S. The Use of Pascal-like Triangles in Describing First Order NMR Coupling Patterns. *J. Chem. Educ.* **1987**, *64*, 315.
- (65) Sharp, R. R. Rotational Diffusion and Magnetic Relaxation of  $^{119}\text{Sn}$  in Liquid  $\text{SnCl}_4$  and  $\text{SnI}_4$ . *J. Chem. Phys.* **1972**, *57*, 5321–5330.
- (66) Grondona, P.; Olivieri, A. C. Quadrupole Effects in Solid-State NMR Spectra of Spin- $\frac{1}{2}$  Nuclei: A Perturbation Approach. *Concepts Magn. Reson.* **1993**, *5*, 319–339.

- (67) Jung, M.-C.; Raga, S. R.; Qi, Y. Properties and Solar Cell Applications of Pb-Free Perovskite Films Formed by Vapor Deposition. *RSC Adv.* **2016**, *6*, 2819–2825.
- (68) Li, B.; Long, R.; Xia, Y.; Mi, Q. All-Inorganic Perovskite CsSnBr<sub>3</sub> as a Thermally Stable, Free-Carrier Semiconductor. *Angew. Chemie Int. Ed.* **2018**, *57*, 13154–13158.
- (69) Tao, S.; Schmidt, I.; Brocks, G.; Jiang, J.; Tranca, I.; Meerholz, K.; Olthof, S. Absolute Energy Level Positions in Tin- and Lead-Based Halide Perovskites. *Nat. Commun.* **2019**, *10*, 2560.
- (70) Nakatsuji, H. *Nuclear Magnetic Shieldings and Molecular Structure*; Tossell, J. A., Ed.; Springer Netherlands: Dordrecht, 1993.
- (71) Dmitrenko, O.; Bai, S.; Dybowski, C. Prediction of <sup>207</sup>Pb NMR Parameters for the Solid Ionic Lead(II) Halides Using the Relativistic ZORA-DFT Formalism: Comparison with the Lead-Containing Molecular Systems. *Solid State Nucl. Magn. Reson.* **2008**, *34*, 186–190.
- (72) Yamada, K.; Isobe, K.; Okuda, T.; Furukawa, Y. Successive Phase Transitions and High Ionic Conductivity of Trichlorogermanate (II) Salts as Studied by <sup>35</sup>Cl NQR and Powder X-Ray Diffraction. *Zeitschrift für Naturforsch. A* **1994**, *49*, 258–266.
- (73) Weber, D. CH<sub>3</sub>NH<sub>3</sub>SnBr<sub>x</sub>I<sub>3-x</sub> (x = 0-3), Ein Sn(II)-System Mit Kubischer Perowskitstruktur. *Z. Naturforsch.* **1978**, *33b*, 862–865.
- (74) Onoda, N.; Yamamuro, O.; Matsuo, T.; Suga, H.; Oikawa, K.; Tsuchiya, N.; Kamiyama, T.; Asano, H. Neutron-Diffraction Study of CD<sub>3</sub>ND<sub>3</sub>SnBr<sub>3</sub>: Semiconductor-Insulator Transition with Orientational Ordering. *Phys. B* **1995**, *213-214*, 411–413.
- (75) Yamada, K.; Isobe, K.; Tsuyama, E.; Okuda, T.; Furukawa, Y. Chloride Ion Conductor CH<sub>3</sub>NH<sub>3</sub>GeCl<sub>3</sub> Studied by Rietveld Analysis of X-Ray Diffraction and <sup>35</sup>Cl NMR. *Solid State Ion.* **1995**, *79*, 152–157.
- (76) Chung, I.; Lee, B.; He, J.; Chang, R. P. H.; Kanatzidis, M. G. All-Solid-State Dye-Sensitized Solar Cells with High Efficiency. *Nature* **2012**, *485*, 486–489.
- (77) Mancini, A.; Quadrelli, P.; Milanese, C.; Patrini, M.; Guizzetti, G.; Malavasi, L. CH<sub>3</sub>NH<sub>3</sub>Sn<sub>x</sub>Pb<sub>1-x</sub>Br<sub>3</sub> Hybrid Perovskite Solid Solution: Synthesis, Structure, and Optical Properties. *Inorg. Chem.* **2015**, *54*, 8893–8895.
- (78) Leijtens, T.; Prasanna, R.; Gold-Parker, A.; Toney, M. F.; McGehee, M. D. Mechanism of Tin Oxidation and Stabilization by Lead Substitution in Tin Halide Perovskites. *ACS Energy Lett.* **2017**, *2*, 2159–2165.
- (79) Wang, F.; Ma, J.; Xie, F.; Li, L.; Chen, J.; Fan, J.; Zhao, N. Organic Cation-Dependent Degradation Mechanism of Organotin Halide Perovskites. *Adv. Funct. Mater.* **2016**, *26*, 3417–3423.
- (80) Wrackmeyer, B. Application of <sup>119</sup>Sn NMR Parameters. *Annu. Rep. NMR Spectrosc.* **1999**, *38*, 203–264.

- (81) Kubicki, D. J.; Prochowicz, D.; Salager, E.; Rakhmatullin, A.; Grey, C. P.; Emsley, L.; Stranks, S. D. Local Structure and Dynamics in Methylammonium, Formamidinium, and Cesium Tin(II) Mixed-Halide Perovskites from  $^{119}\text{Sn}$  Solid-State NMR. *J. Am. Chem. Soc.* **2020**, *142*, 7813–7826.
- (82) Bloembergen, N.; Rowland, T. J. On the Nuclear Magnetic Resonance in Metals and Alloys. *Acta Metall.* **1953**, *1*, 731–746.
- (83) Borsa, F.; Barnes, R. G. Temperature Dependence of the Isotropic and Anisotropic Knight Shift in Polycrystalline Cadmium and  $\beta$ -Tin. *J. Phys. Chem. Solids* **1966**, *27*, 567–573.
- (84) Michaelis, V. K.; Griffin, R. G.; Corzilius, B.; Vega, S. *Handbook of High Field Dynamic Nuclear Polarization*, 1st ed.; Michaelis, V. K., Griffin, R. G., Corzilius, B., Vega, S., Eds.; Wiley, 2020.
- (85) Ha, M.; Michaelis, V. K. High-Frequency Dynamic Nuclear Polarization NMR for Solids: Part 1 – An Introduction. In *Modern Magnetic Resonance*; Springer International Publishing: Cham, 2017; pp 1–24.
- (86) Ha, M.; Michaelis, V. K. High-Frequency Dynamic Nuclear Polarization NMR for Solids: Part 2 – Development and Applications. In *Modern Magnetic Resonance*; Springer International Publishing: Cham, 2017; pp 1–18.
- (87) Michaelis, V. K.; Kroeker, S.  $^{73}\text{Ge}$  Solid-State NMR of Germanium Oxide Materials: Experimental and Theoretical Studies. *J. Phys. Chem. C* **2010**, *114*, 21736–21744.
- (88) Robinson, K.; Gibbs, G. V.; Ribbe, P. H. Quadratic Elongation: A Quantitative Measure of Distortion in Coordination Polyhedra. *Science*. **1971**, *172*, 567–570.
- (89) Fleet, M. E. Distortion Parameters for Coordination Polyhedra. *Mineral. Mag.* **1976**, *40*, 531–533.
- (90) Prasanna, R.; Leijtens, T.; Dunfield, S. P.; Raiford, J. A.; Wolf, E. J.; Swifter, S. A.; Werner, J.; Eperon, G. E.; de Paula, C.; Palmstrom, A. F.; et al. Design of Low Bandgap Tin–Lead Halide Perovskite Solar Cells to Achieve Thermal, Atmospheric and Operational Stability. *Nat. Energy* **2019**, *4*, 939–947.
- (91) Lin, R.; Xiao, K.; Qin, Z.; Han, Q.; Zhang, C.; Wei, M.; Saidaminov, M. I.; Gao, Y.; Xu, J.; Xiao, M.; et al. Monolithic All-Perovskite Tandem Solar Cells with 24.8% Efficiency Exploiting Comproportionation to Suppress Sn(II) Oxidation in Precursor Ink. *Nat. Energy* **2019**, *4*, 864–873.
- (92) Zhao, D.; Chen, C.; Wang, C.; Junda, M. M.; Song, Z.; Grice, C. R.; Yu, Y.; Li, C.; Subedi, B.; Podraza, N. J.; et al. Efficient Two-Terminal All-Perovskite Tandem Solar Cells Enabled by High-Quality Low-Bandgap Absorber Layers. *Nat. Energy* **2018**, *3*, 1093–1100.
- (93) Wasylshen, R. E.; Knop, O.; Macdonald, J. B. Cation Rotation in Methylammonium Lead Halides. *Solid State Commun.* **1985**, *56*, 581–582.

